Linear and nonlinear stability of hydrothermal waves in planar liquid layers driven by thermocapillarity

Linear and non-linear stability of hydrothermal waves in planar liquid layers driven by thermocapillarity

P. J. Sáenz,[1] P. Valluri,[1,a)] K. Sefiane,[1] G. Karapetsas,[2] and O. K. Matar[3]

[1]*Institute for Material and Processes, University of Edinburgh, Edinburgh, EH9 3JL, UK*

[2]*Department of Mechanical Engineering, University of Thessaly, Volos, GR-38334, Greece*

[3]*Department of Chemical Engineering, Imperial College London, London, SW7 2AZ, UK*

ABSTRACT

A shallow planar layer of liquid bounded from above by gas is set into motion via the thermocapillary effect resulting from a thermal gradient applied along its interface. Depending on the physical properties of the liquid and the strength of the gradient, the system is prone to departure from its equilibrium state and to the consequent development of an oscillatory regime. This problem is numerically investigated for the first time by means of two-phase direct numerical simulations fully taking into account the presence of a deformable interface. Obliquely-travelling hydrothermal waves (HTWs), similar to those first described by Smith and Davis (1983) [Smith, M.K. and S.H. Davis, Instabilities of Dynamic Thermocapillary Liquid Layers .1. Convective Instabilities. Journal of Fluid Mechanics, 1983. 132(Jul): p. 119-144], are reported presenting good agreement with linear stability theory and experiments. The non-linear spatio-temporal growth of the instabilities is discussed extensively along with the final bulk flow for both the liquid and gas phases. Our study reveals the presence of interface deformations which accompany the HTWs pattern with a certain time-delay. The local heat fluxes are found to be significantly affected by the transient nature of the HTWs, contradicting the results of previous single-phase studies.

[a)] Corresponding author: prashant.valluri@ed.ac.uk

I. INTRODUCTION

At the beginning of the twentieth century, Bénard [1] performed a series of experiments in which a horizontal liquid layer was subjected to a vertical temperature gradient and found regular cellular convection patterns (Bénard cells). Motivated by Bénard's results, Rayleigh [2] completed a fundamental theoretical study focusing on instabilities of liquid layers due to buoyancy. Pearson [3] examined drying paint films and pointed out the presence of steady convective cells of similar to those observed by Bénard even when the free surface was inverted (and, therefore, the gravity vector was effectively reversed). Since the instabilities seemed to be unaffected by the direction of gravitational field, Pearson concluded that these patterns could not be explained by means of density gradients and proposed surface tension gradients as the principal driving force, i.e. the *Marangoni effect*. Following a similar approach to that performed by Lord Rayleigh, Pearson carried out a linear stability analysis on a horizontal liquid layer of depth d subjected to the vertical temperature gradient resulting from the supply of heat to the lower plate. He regarded surface tension σ as a linearly decreasing function of temperature, $\gamma = -\partial\sigma/\partial T$, ignored the effects of the gas phase, assumed a fixed non-deformable interface and isolated capillary convection from buoyancy by neglecting gravity. Pearson expressed the critical conditions for the onset of convective instabilities by means of the Marangoni number $Ma = \gamma b d^2/\mu\alpha$ (he referred to it as the generic dimensionless number B) where b is the thermal gradient, μ is the dynamic viscosity and α is the thermal diffusivity. Scriven and Sterling [4] extended Pearson's stability analysis by taking into account free-surface deformations and provided a criterion to distinguish whether buoyancy or surface tension dominate cellular convection in liquid pools [4].

Smith and Davis [5, 6] employed linear theory to investigate the stability of liquid film of small depth for two different planar geometries whose basic-state solutions are referred to as the "linear-flow" solution (infinite liquid layer) and the "return-flow" solution (two-dimensional slot). In the first part of their work [5], the authors considered the effect of three-dimensional disturbances for a fluid with constant physical properties, and a surface tension linearly-dependent on temperature set into motion by a horizontal thermal gradient imposed along the interface. The free-surface is regarded as non-deformable, the dynamics of the gas phase is neglected, the liquid is bounded from below by an adiabatic rigid plane and there are no body forces. Heat transfer across the interface is controlled through the Biot number $B = hd/k$ where h is a heat transfer coefficient, d is the layer thickness, and k is the liquid

thermal conductivity. Smith and Davis [5] found two classes of thermal-convective instabilities, namely *stationary longitudinal rolls* and *propagating hydrothermal waves* (hereafter referred to as HTWs). The former type is basically the classical instability studied by Pearson [3] whereas the latter represents a different mode of instability. They also used the Ma number to define the onset of the instabilities and, analogously to Pearson [3], discovered that the most unstable case always corresponds to the adiabatic interface, i.e. $B = 0$. For the linear-flow solution, the preferred mode consists of two HTWs propagating at angles $\pm\psi$ with respect to the axis opposite to the direction of the surface flow when $Pr < 0.60$; a single two-dimensional HTW propagating in parallel to the basic state flow when $0.60 < Pr < 1.60$ and stationary longitudinal rolls for $Pr > 1.60$; here Pr corresponds to the Prandtl number. In the return-flow configuration the preferred mode is always a HTW propagating at angles $\pm\psi$ with respect to the axis opposite to the direction of the surface flow. The angle of propagation for oblique HTWs is solely a function of *Pr*.

In the second part of their investigation [6], Smith and Davis focused on a different family of thermocapillary instabilities, the so-called "surface-wave" instabilities, whose mechanism is critically connected to significant interface deformations. Since we are primarily interested in the HTWs, we do not go into the details of this topic and refer the reader to [6] for further information. An extensive review on thermocapillary instabilities was performed by Davis [7]. In a subsequent paper, Smith [8] described the physical mechanisms of the new HTW instability. At small Pr numbers, the HTWs extract their energy from the externally-imposed horizontal temperature gradient by the streamwise flow whereas, at large Pr numbers, the energy is obtained from the flow-induced vertical temperature field by vertical convection [8]. It is worth highlighting the work of other authors who extended the theoretical study by Smith and Davis to account for buoyancy effects, namely Garr-Peters [9, 10]; Parmentier *et al.* [11]; Mercier and Normand [12] and more recently Chan and Chen [13]. Parmentier *et al.* [11] confirmed the always stabilizing effect of viscosity and noticed that the system's behaviour was decisively connected to the Pr number. They concluded that it could only be guaranteed that buoyancy destabilizes the flow when $Pr > 2.6$. However, if $Pr < 0.4$, the effect is inverted and gravity tends to stabilize the system. Mercier and Normand [12] investigated the transition between stationary and oscillatory modes, which depends on the relative importance of buoyancy and capillary forces, and reported two new types of oscillatory modes presenting significant differences with the predictions by Smith and Davis [5]. Chan and Chen [13] observed a slight increment in the angle of propagation

when the effect of gravity is weak until a inflexion point from which the angle decreases steadily to zero. The phase-speed and wavelength decrease constantly as the role of gravity becomes more predominant.

Numerous experimental investigations have been carried out in rectangular [14, 15] and annular geometries [16-18] to study thermocapillary- and buoyancy-driven instabilities but only few of them provide conclusive proof of the existence of HTWs predicted by Smith and Davis [5]. Here we only present the most relevant studies and refer the reader to Schatz and Neitzel [19] and Burguete *et al.* [15] for more detailed reviews. Riley and Neitzel [14] argued that, due to buoyancy and geometric effects, previous experimental studies do not provide a definitive proof for the existence of the HTWs. Hence, they conducted a series of experiments in a laterally-heated rectangular geometry, considering very thin liquid layers of 1cSt silicone oil ($d = 0.75 - 2.5$ mm; $Pr = 13.9$). They reported observing pure HTWs for $d \leq 1.25$ mm presenting good agreement with the results from the linear theory of Smith and Davis [5]. Burguete *et al.* [15] performed similar experiments in a wider rectangular cavity with 0.65cSt silicone oil. They also considered a larger range of liquid heights ($d = 0.5 - 10$ mm) and investigated the influence of the geometrical aspect ratios. Burguete *et al.* [15] observe oblique HTWs and longitudinal stationary rolls for small ($d \leq h_r$) and large ($d > h_r$) fluid depths respectively. Within the HTW regime, for larger heights ($h_c < d < h_r$) the HTW source is a line and generally evolves towards one end of the container leaving a single wave, whereas for smaller heights ($d < h_c$), the source looks like a point and emits a circular wave which becomes almost planar farther from the source in both directions [15]. The transition liquid depths, h_r and h_c, are found to be dependent on cavity's aspect ratio.

With the aims of contrasting previous theoretical and experimental works as well as providing further characterizations of thermocapillary driven flows, HTWs have also been studied by means of numerical simulations. Xu and Zebib [20] conducted 2D and 3D numerical investigations on rectangular cavities for fluids with $1 \leq Pr \leq 13.9$ and obtained neutral stability diagrams. In 2D, the authors also provided results illustrating the influence of the driving force (Re) and streamwise length aspect ratio on the flow structure. In 3D, their attention was focused on the influence of the sidewalls which, in general, had a damping effect on the oscillation. Bucchignani [21] investigated numerically the flow represented by the experiments of Riley and Neitzel [14] on shallow silicone layers ($d = 1$ mm). The author reported temperature and velocity oscillatory perturbations consistent with the observation of

pure HTWs. Taking Schwabe *et al.* [17] as point of reference, several analogous investigations have been carried out on annuli [22-27] showing spiral-like HTW trains consistent with Smith and Davis [5], the HTW deformations result from the annular geometry. Some of the authors also investigate other families of instabilities found when the liquid depth is increased, i.e. when buoyancy becomes the leading force. The emergence of HTWs on a slightly different system was studied very recently by Karapetsas *et al.* [28] who considered the stability of evaporating droplets on a heated substrate. In their case the thermal gradient was not imposed externally but was induced by the evaporation process. The results of their energy analysis showed that the induced waves, which have been also reported in earlier experimental studies [29], are of hydrothermal nature and share exactly the same mechanisms as those described in Smith [8].

All of the aforementioned numerical studies employ a qualitatively similar methodology which shares the same simplifications. The authors completely ignore the gas phase above the liquid layer, use a single-phase model whose upper boundary is regarded as non-deformable (with the exception of the stability analyses by Scriven and Sterling [4], Smith and Davis [5] Karapetsas *et al.* [28]) horizontal free-surface and, if considered, model the heat transfer across the interface via the Biot number and the temperature jump between the free surface and a reference temperature; in most cases the reference temperature is taken to be a constant with the exception of Mercier and Normand [12] who consider instead a profile that varies linearly in the streamwise direction, and Mancho and Herrero [30] who take into account the effect of lateral heating walls. We propose a new two-phase, numerical approach based on the Volume-of-Fluid method, which permits a more realistic direct numerical simulation of thermocapillary flows. As we explain in subsequent sections, our model solves both liquid and gas phases accounting for interface deformations and computes the energy exchange between phases based on the local conditions solely. We demonstrate the development of HTWs over a range of system parameters, and discuss, in detail, the associated interfacial and heat transfer dynamics.

The rest of this paper is organised as follows. In section II, we provide details of the problem formulation and of the numerical techniques used to carry out the computations. Section III is devoted to the description and the discussion of our findings. We start by confirming the base state to then continue presenting the spatio-temporal evolution of the HTWs, the interface deformations induced by the instabilities and the Fourier analyses performed to characterize the oscillatory signals. The section concludes showing the

multiphase bulk flow features along with the explanation of the mechanism of heat transfer across the interface. Finally, the most important conclusions resulting from this investigation are summarized in section IV.

II. PROBLEM STATEMENT AND FORMULATION

A. Problem statement

We study the two-phase thermocapillary flow for a rectangular cavity similar to that employed in Riley and Neitzel [14] (hereafter, referred to as RN). A sketch of the planar model is shown in FIG. 1. The rectangular pool of width W, length L and total height H is filled with a liquid layer of depth d, bounded from above by a gas. A rectangular coordinates system, $(\hat{x}, \hat{y}, \hat{z})$, as shown in FIG. 1, is used to model the flow which is set into motion via a temperature gradient imposed along the interface by fixing the temperature of the end-walls located at $\hat{x} = \pm L/2$. The temperature difference between walls is $\Delta T = T_h - T_c$. The mean temperature $(T_h + T_c)/2$ is chosen to be the reference temperature T_r at which all the physical properties of the fluids are measured.

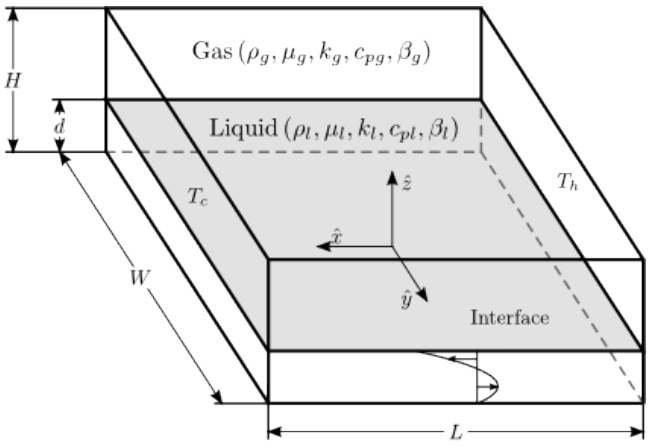

FIG. 1. Sketch of the flow geometry.

Both fluids present in the system are incompressible, viscous and immiscible. The density, dynamic viscosity, thermal conductivity, specific heat capacity and coefficient of thermal expansion are respectively ρ_l, μ_l, k_l, c_{pl}, β_l for the liquid and ρ_g, μ_g, k_g, c_{pg}, β_g for the gas. The surface tension σ is assumed to be a linear function of temperature, i.e. $\hat{\sigma} = \sigma_r -$

$\gamma\left(\hat{T}-T_r\right)$ where $\gamma=-\partial\hat{\sigma}/\partial\hat{T}$ is the temperature coefficient of the surface tension and σ_r is the surface tension at the reference temperature T_r. Evaporation of the liquid layer is considered to be negligible and is ignored.

We introduce the following scalings to calculate the principal dimensionless variables (without carets),

$$\hat{\boldsymbol{x}}=d\boldsymbol{x} \qquad \hat{\boldsymbol{u}}=\frac{\gamma\Delta T}{\mu_l}\boldsymbol{u} \qquad \hat{p}=\frac{\gamma\Delta T}{d}p$$
$$\hat{T}=T\,\Delta T+T_r \qquad \hat{t}=\frac{\mu_l d}{\gamma\Delta T}t \qquad \hat{\sigma}=\sigma_r\,\sigma \tag{1}$$

where $\boldsymbol{x}=(x,y,z)$ and $\boldsymbol{u}=(u,v,w)$ are the coordinate and velocity vectors with respect to the Cartesian system of coordinates located in the centre of the domain; p, T and t denote the pressure, temperature and time, respectively. As a result of this change of variables, the following dimensionless parameters arise,

$$Re=\frac{\gamma d\Delta T}{\mu_l\nu_l} \qquad Fr=\frac{\gamma^2\Delta T^2}{gd\mu_l^2} \qquad We=\frac{\gamma^2\Delta T^2 d}{\mu_l\nu_l\sigma_r} \qquad Pr=\frac{\nu_l}{\alpha_l} \tag{2}$$

Here, $\nu_l=\mu_l/\rho_l$ and $\alpha_l=k_l/\left(\rho_l c_{pl}\right)$ are the liquid kinematic and thermal diffusivities; g is the gravitational acceleration and Re, Fr, We and Pr are the Reynolds, Froude, Weber and Prandtl numbers, respectively. Note that in the above definition we use as characteristic velocity the thermocapillary velocity $\gamma\Delta T/\mu_l$.

Other important dimensionless groups that characterize non-isothermal multiphase flows are the dynamic Bond number Bo_d and the Marangoni number Ma_L:

$$Bo_d=\frac{\rho_l g\beta_l d^2}{\gamma} \qquad Ma_L=\frac{\gamma\Delta T d}{\mu_l\alpha_l} \tag{3}$$

The dynamic Bond number measures the relative importance of thermogravity forces with respect to thermocapillary forces. When Bo_d approaches zero, thermogravity forces are negligible compared to surface tension forces. The Marangoni number is the parameter used to quantify the strength of the thermocapillary convection arising for systems with variable

interfacial tension. Previous works are not consistent regarding the dimensionless framework employed: the definition of the Marangoni number is different in almost every case, based on the suitability of the case considered. For the sake of consistency and enabling easier comparisons, we use our definition of the Marangoni number as expressed in (3) to identify the different cases that we study but employ the *effective* Marangoni number Ma as defined by Smith and Davis [5] (hereafter, referred to as SD) to interpret the results and compare them with other investigations,

$$Ma = \frac{\gamma d^2 b_i}{\mu_l \alpha_l} \tag{4}$$

where $b_i = -\left(d\hat{T}/d\hat{x}\right)$ is the *interior* or *effective* thermal gradient, i.e. the thermal gradient in the core region of the gas-liquid interface. As we shall see when we discuss the implications of the thermal boundary-layers at the end-walls, it is important to highlight that in general $b_i \neq \Delta T/L$. Burguete *et al.* [15] experimentally investigated the extension of the thermal boundary-layers for different liquid depths and observed that these quantities are only equal in situations wherein the Marangoni effects are dominant over buoyancy. The authors reports differences as large as $b_i \cong 0.2\,\Delta T/L$ as the liquid depth increases, which indicates that the use of Ma to characterise the thermal forcing is only appropriate in situations wherein d is small enough for buoyancy effects to be negligible. Note that $Ma = Ma_L \cdot (b_i d/\Delta T)$. For the same reason in order to compare our velocity, temperature and time values with those reported by SD [5], we need to multiply our values of $\boldsymbol{u}$ and T by (Ma_L/Ma) to convert them to the SD scale, whereas t requires multiplying by the inverse factor (Ma/Ma_L).

Since we choose the liquid as reference for the dimensional analysis, the physical properties of the gas are taken into account by means of the following ratios,

$$\Gamma_\rho = \frac{\rho_l}{\rho_g} \qquad \Gamma_\mu = \frac{\mu_l}{\mu_g} \qquad \Gamma_k = \frac{k_l}{k_g} \qquad \Gamma_{c_P} = \frac{c_{pl}}{c_{pg}} \qquad \Gamma_\beta = \frac{\beta_l}{\beta_g} \tag{5}$$

B. Governing equations

In the present work, we make use of the Volume-of-Fluid (VOF) method initially described by Hirt and Nichols [31]. We do not attempt to explain all the details surrounding this technique here and, therefore, refer the reader to Scardovelli and Zaleski [32] for a comprehensive review of the VOF and other methods employed to simulate interfacial flows. This is a well-established method that has been used with success by several researchers in the past for the study of thermocapillary driven flows [33-35].

The VOF approach belongs to the class of *interface-capturing methods* which do not define the interface as a sharp boundary. Instead, the interface between the fluids is a *diffuse region* of finite thickness reconstructed by solving the advection transport of a scalar field, sometimes called colour function. We employ the liquid volume fraction c defined as the volume of liquid phase divided by the total volume of the control volume.

$$c = \begin{cases} 1, & \text{cells filled with liquid} \\ 0, & \text{cells filled with gas} \end{cases} \tag{6}$$

Thus, the interface is the transition region where $0 < c < 1$. The volume fraction is transported across the domain by the conservation equation,

$$\frac{\partial c}{\partial t} + \nabla \cdot (c\boldsymbol{u}) = 0 \tag{7}$$

In a two-phase system only one conservation equation needs to be solved as the volume fraction for the gas phase is simply $(1 - c)$. We use the *one-fluid variant* of the VOF method which treats both liquid and gas as a single fluid whose physical properties vary spatially according to c. This formulation allows computing both incompressible Newtonian fluids using the divergence-free condition (continuity equation) and a single set of momentum equations,

$$\nabla \cdot \boldsymbol{u} = 0 \tag{8}$$

$$\frac{\partial(\rho\boldsymbol{u})}{\partial t} + \nabla \cdot (\rho\boldsymbol{u}\boldsymbol{u}) = \frac{1}{Re}[-\nabla p + \nabla \cdot \mu(\nabla\boldsymbol{u} + \nabla\boldsymbol{u}^T)] + \mathbf{f_b} + \frac{1}{We}\mathbf{f_{sv}} \tag{9}$$

where $\boldsymbol{u}$ and p denote the shared velocity and pressure fields and $\rho = c + (1-c)/\Gamma_\rho$ and $\mu = c + (1-c)/\Gamma_\mu$ are the single-fluid volume-averaged density and viscosity. The volumetric forces $\mathbf{f_b}$ and $\mathbf{f_{sv}}$ account for buoyancy and surface tension respectively.

RN [14] pointed out that buoyancy in the liquid phase cannot be disregarded if one aims to provide a conclusive and accurate description of physically-realisable HTWs. We also intend to investigate the gas flow wherein the same phenomenon becomes important due to the irregular temperature distribution produced by the externally imposed gradient. Following Boussinesq's approximation, the basic idea of our approach is to consider constant the density of the pure substances (ρ_l and ρ_g) everywhere in the momentum equation except for the gravity term, where the densities are approximated by linear functions of T. The application of this approach results in the volumetric force $\mathbf{f_b}$,

$$\mathbf{f_b} = -\rho\left(\frac{1}{Fr} - \frac{Bo_d}{Re}\beta T\right)\mathbf{e_z} \tag{10}$$

where $\beta = c + (1-c)/\Gamma_\beta$ is the single-fluid coefficient of thermal expansion, T is the temperature and $\mathbf{e_z}$ is the unit vector in the vertical direction. Note that this expression reduces to $\mathbf{f_b} = -\left(\frac{1}{Fr} - \frac{Bo_d}{Re}T\right)\boldsymbol{e_z}$ in the bulk of the liquid ($c = 1$) and to $\mathbf{f_b} = -\frac{1}{\Gamma_\rho}\left(\frac{1}{Fr} - \frac{Bo_d}{Re}\frac{1}{\Gamma_\beta}T\right)\boldsymbol{e_z}$ in the gas ($c = 0$), which in dimensional terms is $\hat{\mathbf{f}}_\mathbf{b} = -\left[\rho_l - \rho_l\beta_l\left(\hat{T} - T_r\right)\right]g\boldsymbol{e_z}$ and $\hat{\mathbf{f}}_\mathbf{b} = -\left[\rho_g - \rho_g\beta_g\left(\hat{T} - T_r\right)\right]g\boldsymbol{e_z}$, respectively.

Surface tension effects are incorporated in the momentum balance by means of the Continuum Surface Force (CSF) model formulated by Brackbill *et al.* [36]. Contrary to other sharp-interface approaches where the surface tension is a superficial force applied as a discrete boundary condition, the essential idea underlying the CSF model is the computation of the surface tension as a smoothly-varying volumetric force acting on the transition region between phases. The conservation of momentum gives the classical surface tension force per unit of interfacial area, $\mathbf{f_{sa}}$,

$$\mathbf{f_{sa}} = \sigma\kappa\mathbf{n} + \nabla_s\sigma \tag{11}$$

where σ is the surface tension; $\kappa = -(\nabla_s \cdot \mathbf{n})$ denotes the interface curvature; $\mathbf{n} = \nabla c/|\nabla c|$ is the unit vector normal to the interface pointing from the gas to the liquid and $\nabla_s = \nabla -$

$\mathbf{n}(\mathbf{n}\cdot\nabla)$ is the gradient operator tangent to the interface. The first term in (11) represents the force normal to the interface proportional to the surface tension coefficient σ and the curvature κ (Laplace's formula). The second term is a force tangent to the interface that arises only in cases in which the surface tension varies spatially giving rise to thermocapillary-driven flows. In dimensionless form, the linear dependency between σ and T takes the form,

$$\sigma = 1 - Ca\,T \tag{12}$$

where Ca is the capillary number defined as $Ca = \gamma\Delta T/\sigma_r$. The reader should note that Ca, which represents the ratio of viscous force to surface tension force, is not a new independent dimensionless number and can be obtained as $Ca = We/Re$.

In accordance with the CSF model, the force per unit interface area $\mathbf{f_{sa}}$ is converted into a force per unit volume $\mathbf{f_{sv}}$ via $\delta = |\nabla c|$ which takes a finite value at the interface and 0 elsewhere.

$$\mathbf{f_{sv}} = (\sigma\kappa\mathbf{n} + \nabla_s\sigma)\delta \tag{13}$$

When we employ equation (12) for the tangential term in (13), we obtain

$$\mathbf{f_{sv}} = (\sigma\kappa\mathbf{n} - Ca\nabla_s T)\delta \tag{14}$$

Substitution of equations (10) and (14) in (9) and small rearrangements in the surface-tension term yield the final expression of the momentum equation,

$$\frac{\partial(\rho\boldsymbol{u})}{\partial t} + \nabla\cdot(\rho\boldsymbol{u}\boldsymbol{u}) = \frac{1}{Re}[-\nabla p + \nabla\cdot\mu(\nabla\boldsymbol{u} + \nabla\boldsymbol{u}^T)] - \rho\left(\frac{1}{Fr} - \frac{Bo_d}{Re}\beta T\right)\mathbf{e_z} + \left(\frac{1}{We}\sigma\kappa\mathbf{n} - \frac{1}{Re}\nabla_s T\right)\delta \tag{15}$$

The model is completed with the equation for the conservation of energy in its temperature form. Ignoring pressure and viscous dissipations, the governing equation can be written as follows,

$$\frac{\partial(\rho c_p T)}{\partial t} + \nabla\cdot(\rho c_p T\boldsymbol{u}) = \frac{1}{Ma_L}\nabla\cdot(k\nabla T) \tag{16}$$

where T is the shared temperature field, k denotes the thermal conductivity calculated by $k = c + (1 - c)/\Gamma_k$ and c_p is the mass-averaged heat capacity computed as $c_p = \frac{c+(1-c)/(\Gamma_\rho \Gamma_{cp})}{c+(1-c)/\Gamma_\rho}$.

The governing equations (7), (8), (15) and (16) form the set of six PDEs with six unknowns (c, u, v, w, p and T) solved numerically via the finite-volume method. Derivatives in diffusion terms are approximated by the centered scheme while a second-order upwind scheme is employed for the advection terms. The reconstruction of the interface is accomplished via a classical compressive differencing scheme similar to that of Ubbink [37]. The solution is advanced in time with the implicit second-order backward Euler method. Convergence at each time step is assumed when the root-mean-square (RMS) residual is below the target value 1×10^{-5}. The timestep size is selected so that it is always smaller than the viscous, conductive and Maragoni timescales, i.e. $\Delta t < \min(\Delta x^2/\nu_l\,;\ \Delta x^2/\alpha_l\,;\ \Delta x/u_0)$. In all the cases presented in this work, the Marangoni timescale ($O(10^{-3}$ s)) is the leading criterion which is logical given that thermocapillary advection is the system's fundamental driving force. The Marangoni timescale also satisfies the low Courant number criterion necessary for the compressive differencing scheme used. The physical domain is discretized by means of a hexahedral mesh with the scalar variables stored in the cells centres and the velocities at the cell faces (staggered grid). Special attention is paid to the correct resolution of the thermal boundary-layers near the fixed-temperature walls. To that end, we employ a biased element distribution with finer resolution near the end-walls. The effects of deficiently resolved boundary-layers are illustrated in more detail section III.A along with the mesh dependency test.

C. Boundary and initial conditions

The rectangular domain is bounded below by a solid wall and in the streamwise direction by vertical fixed-temperature walls. These solid boundaries are all impermeable and the no-slip condition is applied for the momentum equation. In dimensionless form, the domain's height H and the streamwise L and the spanwise W lengths are taken into account by means of the geometrical ratios $A_H = H/d$, $A_L = L/d$ and $A_W = W/d$, respectively. Hence, we can express the previous conditions in mathematical notation as follows,

$$\boldsymbol{u} = (0,0,0) \qquad T = \pm\frac{1}{2} \qquad \text{at} \qquad x = \mp\frac{A_L}{2} \tag{17}$$

$$\boldsymbol{u} = (0,0,0) \qquad \frac{\partial T}{\partial z} = 0 \qquad \text{at} \qquad z = 0 \tag{18}$$

To minimize any end-effects in the spanwise direction, we employ periodic boundary conditions at the sidewalls ($y = \pm A_W/2$). The upper surface ($z = A_H$) is assumed to be a constant-pressure ($p = 0$) open boundary which allows flow into and/or out of the domain. *A priori* unknown, the flow direction is locally calculated based on the direction of the surrounding velocity field. For velocity vectors pointing into the domain, the temperature of the gas is assumed to be at T_r; whereas for flows leaving the domain, zero gradient conditions for velocity and temperature are applied to close the boundary value problem. This open boundary is, therefore, a mixed Dirichlet-Neumann boundary condition.

Initially, we start with a perfectly horizontal interface. To save computational time, we employ the return-flow solution presented by SD [5] as an initial condition for the liquid, whereas the gas starts at rest with the temperature field characteristic of pure steady-state heat conduction in the spanwise direction:

$$\boldsymbol{u} = \frac{c}{A_L}\left(\frac{3z^2 - 2z}{4}, 0, 0\right)$$

$$T = -\frac{1}{A_L}\left[x + c\frac{Ma_L}{48A_L}(3z^4 - 4z^3 + 1)\right] \qquad \text{at} \qquad t = 0 \tag{19}$$

$$p = c\frac{3x}{2A_L}$$

Note that in these expressions we approximate $b_i \simeq \Delta T/L$ because a priori we do not know its value due to the thermal boundary-layer effects at the end-walls.

We can also study wettability effects by defining the contact angle on solid boundaries. The specified angle is then used to calculate the interface normal vector for cells contiguous to the walls, which is later used in the computation of both the curvature and the surface

tension force. For simplicity, we maintain a constant value of 90° in the present work and leave a more in-depth analysis of wettability effects for future studies.

III. RESULTS AND DISCUSSION

A. Base state

We start our investigation of the system dynamics by considering whether a steady-state can be attained for the case of a thin liquid layer with $Pr = 13.9$ and a quiescent gas. The geometrical domain is defined by $A_L = 30$, $A_W = 50$ and $A_H = 3$. Tests were also carried out with $A_H = 6$ and 4 and it was seen that the results were independent of the domain height from $A_H \geq 3$. The remaining dimensionless parameters are: $Re = 755$, $Fr = 58.2$, $We = 27.1$, $Bo_d = 0.142$, $Ma_L = 10500$, $\Gamma_\rho = 688$, $\Gamma_\mu = 44.6$, $\Gamma_k = 3.85$, $\Gamma_{c_p} = 1.71$ and $\Gamma_\beta = 0.4$. Note that these values correspond to the same stable case studied experimentally by RN [14] with a 1-mm liquid layer of 1cSt Dow Corning silicone oil, normal air and $\Delta T = 8.16$ K. SD [5] predict a critical Marangoni number $Ma_c^{SD} = 295$ for this configuration. We should bear in mind that this value has been obtained from a stability analysis that disregards the stabilizing effects of gravity and heat loss across the interface. RN [14] report $Ma_c^{RN} = 366$ for the same system but their critical value is calculated from their experimental work under normal gravity and with the liquid layer open to ambient air. Hence, comparison between Ma_c^{SD} and Ma_c^{RN} gives a quantitative evaluation of the effects of the theoretical simplifications on the stability of the flow.

In the initial stages, the flow undergoes an adjustment period in which the originally imposed temperature gradient $(\Delta T/L)$ is progressively reduced by the effect of the thermal boundary-layers acting at the walls. Once the boundary-layers have been established completely, the system reaches a steady-state wherein velocity and temperature are essentially constant. The steady streamwise temperature profile at the interface is shown in FIG. 2a. At this point, the effective temperature gradient for the core region b_i remains constant but is smaller than that initially imposed because of the evolution of the thermal boundary-layers at the walls. It must be noted that SD [5] did not encounter this due to their unbounded infinite domain. Thus, to correctly interpret our results and compare them with other works, we shall use b_i which is obtained *a posteriori*. We find $Ma = 214$ (calculated

from a fitted value of effective temperature gradient, b_i) which is lower than Ma_c^{SD} and therefore corresponds to a stable configuration whose bulk flow should be similar to the basic state presented in [5].

TABLE I shows that convergence is achieved upon mesh refinement. The simulations are run for large number of timesteps $(3 - 4 \times 10^5)$ before crucial system parameters such as superficial velocity and effective Marangoni number, which measures the effective thermal gradient, are read. Due to the small relative difference in these parameters between $73^x \times 121^y \times 59^z$ and $61^x \times 101^y \times 49^z$ (1.33% for u and 2.01% for Ma), the latter mesh is chosen for further simulations.

TABLE I: Mesh dependency test for the case presented in section A.

Grid	Surface velocity	Effective gradient
$73^x \times 121^y \times 59^z$	$u = 5.6 \times 10^{-3}$	$Ma = 218$
$61^x \times 101^y \times 49^z$	1.33 %	2.01 %
$51^x \times 84^y \times 41^z$	7.23 %	3.56 %
$43^x \times 70^y \times 34^z$	9.42 %	5.58 %

Obtaining well-resolved thermal boundary-layers is vital. FIG. 2b shows the thermal boundary-layer with mesh refinement. At low mesh densities, we observe that the temperature of the liquid right next to the hot wall drops from the fixed value, $T = 0.5$. The opposite behaviour is detected near the cold end. This is indicative of a poorly resolved boundary-layer resulting in a lower effective thermal gradient at the centre. It was noted that for coarse resolutions, the interior gradient reaches a constant value unaffected by ΔT, incorrectly preventing the system from going beyond the critical point and, therefore, from being subjected to any instability mode. The most efficient way to overcome this difficulty is by refining the mesh near the walls. We use $61^x \times 101^y \times 49^z$ with a mesh refinement such that there are at least 6-9 computational points within the boundary regions.

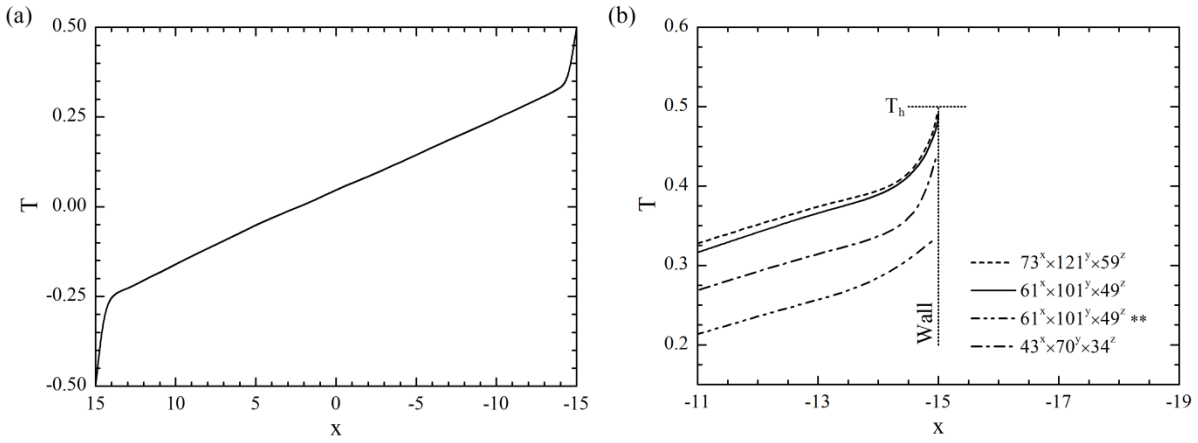

FIG. 2. (a) Steady surface temperature distribution and (b) resolution of the thermal boundary-layer with $Pr = 13.9$, $Re = 755$, $Fr = 58.2$, $We = 27.1$, $Bo_d = 0.142$, $Ma_L = 10500$, $\Gamma_\rho = 688$, $\Gamma_\mu = 44.6$, $\Gamma_k = 3.85$, $\Gamma_{c_p} = 1.71$ and $\Gamma_\beta = 0.4$. The asterisks (**) denotes a uniform element distribution, i.e. no grid refinement near the walls.

Although we compute the full 3D case, we observe that the flow is basically independent of the spanwise direction as expected. In FIG. 3 we compare the numerically obtained base state liquid streamwise velocity (FIG. 3a) and flow-induced temperature fields (FIG. 3b) with those from experiments [14], and those used in the stability analysis of SD [5]; this is done at the domain centre, $y = 0$. Following RN [14], the velocity profile in FIG. 3a has been scaled by the interface value as opposed to the thermocapillary velocity scale. Since RN [14] do not report the vertical temperature distribution for their experiments, in FIG. 3b we only compare our results with the theory of SD [5]. The predicted steady state is thus in good agreement for both the velocity and the temperature fields and these results serve as a good validation of our code, allowing us to continue with a more thorough study of the stability characteristics and the dynamics of this system.

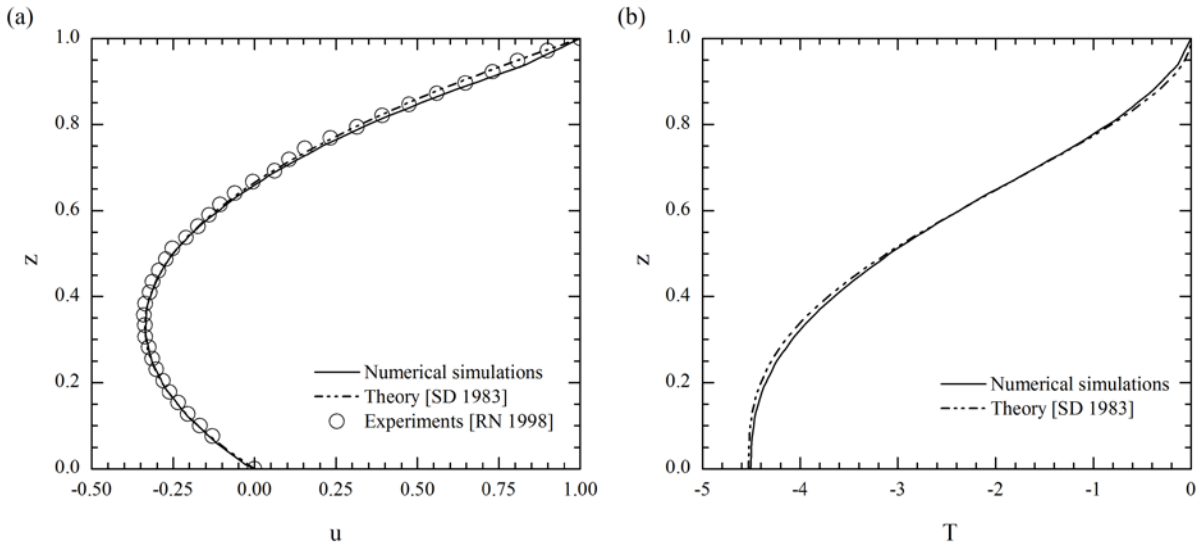

FIG. 3. Basic-state profiles for the liquid at $(x, y) = (0, 0)$; (a) streamwise velocity (b) flow-induced temperature. The parameters are the same as in FIG. 2.

B. Hydrothermal waves

We now choose a liquid with $Pr = 0.75$ and impose a temperature difference between the end-walls large enough to make sure that the effective thermal gradient is supercritical, i.e. the flow is within the unstable region. In this case, the geometrical domain is comparatively smaller only in the spanwise direction, $A_W = 15$. Tests were also conducted with $A_W = 30$ to ensure the independence of the results. We first focus on the case of an adiabatic interface studied by SD [5], and impose a specially large thermal conductivity ratio, $\Gamma_k = 10^{10}$, which effectively means that the gas acts as a thermal insulator. The remaining dimensionless parameters that define the physical system are $Re = 11912$, $Fr = 1726$, $We = 748$, $Bo_d = 0.111$, $Ma_L = 8934$, $\Gamma_\rho = 641$, $\Gamma_\mu = 14.3$, $\Gamma_{c_p} = 2$ and $\Gamma_\beta = 0.4$. Pure HTWs are only found for capillary flows in which surface tension is dominant over gravity; this condition is met when Bo_d approaches zero or, in dimensional terms, when the liquid depth is smaller than the capillary length. Since RN [14] report HTWs for $Bo_d \leq 0.222$ and in the case presented here $Bo_d = 0.111$, we expect to observe the same instability mode. The time-step size and the grid resolution are 0.823 and $101^x \times 61^y \times 49^z$ respectively.

1. Spatio-temporal evolution

The overall transient evolution of the system is analysed by recording the time history of the principal variables for the interface (temperature and velocity) at the mid-point $P_o(0, 0\ z_i)$ as shown in FIG. 4, in which z_i locates the interfaces. Given the deformable interface, the vertical location of this monitoring point, $z_{P_o} = z_i$, is part of the transient solution corresponding to $c = 0.5$ at $x_{P_o} = y_{P_o} = 0$.

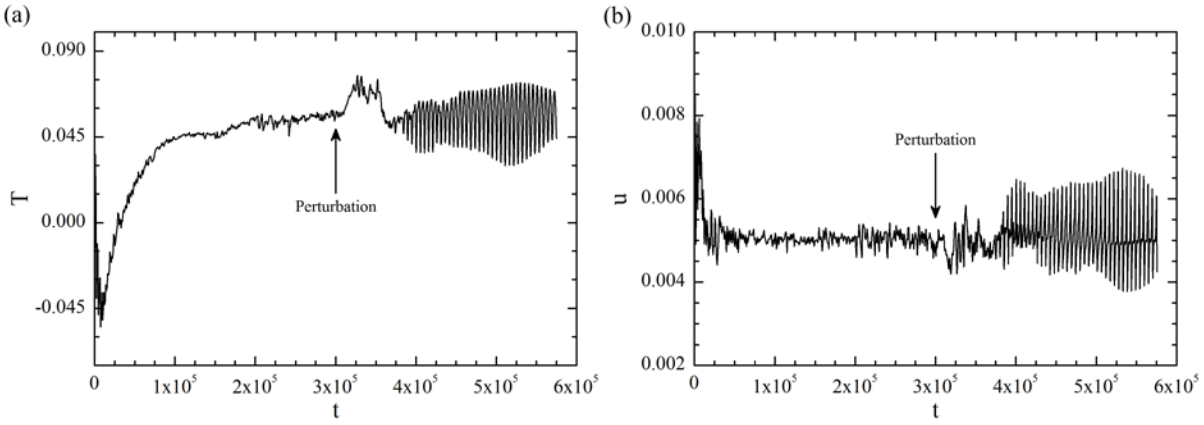

FIG. 4. Instantaneous (a) interface temperature and (b) flow speed for the adiabatic-interface case with $Pr = 0.75$, $Re = 11912$, $Fr = 1726$, $We = 748$, $Bo_d = 0.111$, $Ma_L = 8934$, $\Gamma_\rho = 641$, $\Gamma_\mu = 14.3$, $\Gamma_k = 10^{10}$, $\Gamma_{c_p} = 2$ and $\Gamma_\beta = 0.4$. The monitoring point $P_o = (0, 0, z_i)$ is located at the centre of domain on the interface. Insets showing the dynamics of the oscillatory stage are available in FIG. 9.

FIG. 4a shows the instantaneous temperature distribution at the centre of the interface. The capillary flow first undergoes a strong transient period ($t < 10^5$) wherein its surface temperature initially decays but then quickly recovers, reaching a practically steady-value around $T = 0.045$, slightly higher than the original. This minor deviation, 4.5% of the temperature difference between the end-walls, is attributed to boundary effects resulting from having a finite domain, is related to the adjustment from the imposed initial conditions presented in equation (19) to the numerically-generated 'base state' wherein the thermal boundary-layers have been established. From $t = 1.6 \times 10^5$ to 3×10^5 no noteworthy change is observed in the flow. At $t = 3 \times 10^5$, we introduce a small perturbation over the velocity and the temperature fields. The perturbations' amplitudes are respectively $u_{P_o}/1000$ for the velocity and 10^{-3}, $\Delta T/1000$, for the temperature, where u_{P_o} represents the flow speed recorded by P_o at the interface. The perturbation wavelength and angle of propagation are those provided by SD [5] for the critical mode with *Pr*. In the particular case under

consideration, these criteria result in perturbations of amplitudes 5.1×10^{-6} (velocity) and 10^{-3} (temperature), wavelength 4.18 and angle of propagation 57°. No distinguishable mode manifests itself until $t = 3.7 \times 10^5$, at which time the effects of the HTWs are first captured. The flow then enters the progressively-growing oscillatory state characteristic of an unstable regime.

Similar conclusions can be drawn from the study of the instantaneous evolution of the velocity for the same point. FIG. 4b shows the magnitude of $\boldsymbol{u}$ throughout the numerical simulation. In this case, it is more difficult to identify the same stages as those reported from the temperature profile. The transient period for the speed is approximately 20% of the thermal and it is followed by a quasi-steady state, from $t = 10^5$ to 3×10^5, in which the velocity experiences small deviations from its mean value $u = 0.0051$. The conversion of this average value to the dimensionless framework by SD [5] yields $u = 0.22$ which is in good agreement with the superficial velocity reported by the authors, $u = 0.25$. In this period the spanwise component of the flow velocity does not follow any dominant pattern and it is at least two orders of magnitude smaller than the streamwise component.

FIG. 5a shows the interface temperature distribution at the centre of the planar geometry ($y = 0$) in the streamwise direction for $t = 5.572 \times 10^5$. At this instant, the flow has already gone deep into the oscillatory phase and has reached a quasi-steady-state wherein the prevailing HTW mode is fully-developed throughout the liquid layer. The thermal boundary-layer is more prominent near the cold wall where it causes a sudden temperature drop of approximately 0.25, double the temperature jump existing near the hot boundary. This difference in extension is provoked by surface flow of hot fluid being transported towards the cold wall due to the Marangoni effect. The temperature profile in the core region presents three wave-like deviations from its average linear value.

We compute the effective thermal gradient and find $Ma = 211$, which is higher than the critical value reported by SD [5], $Ma_c^{SD} = 96$, for the same liquid and $B = 0$. The corresponding superficial temperature distribution is shown in FIG. 5b. The isotherms clearly resemble the shape of the HTWs presenting an oblique pattern, which is the projection of the HTW disturbances onto the principal xz plane. The perturbations travel from the lower-left (cold) towards the upper-right corner (hot) in FIG. 5b which is consistent with the results from stability theory that predict HTWs travelling upstream [5, 8].

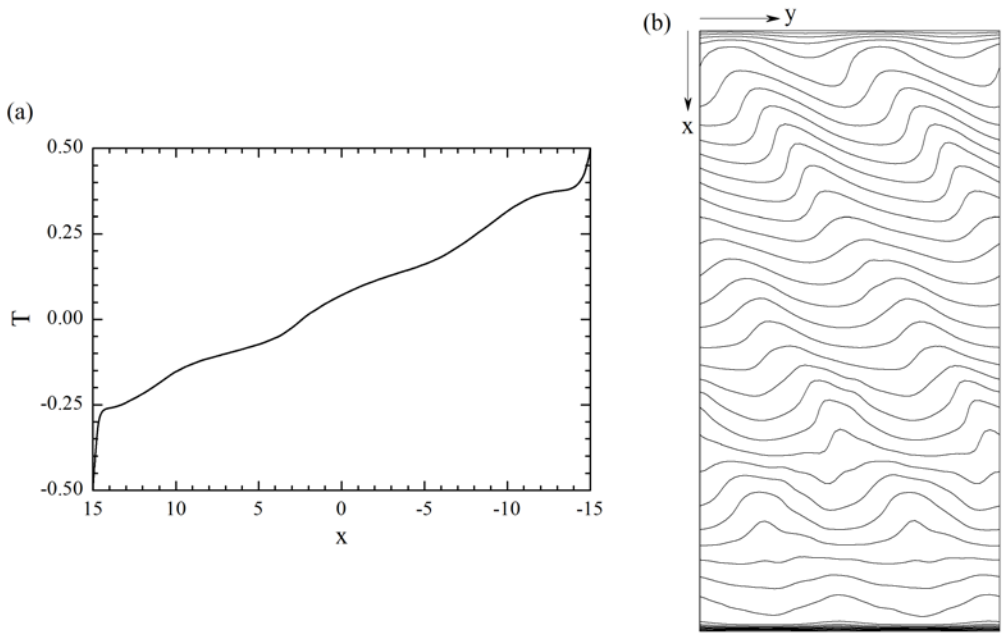

FIG. 5. (a) Streamwise temperature distribution along the interface for $y = 0$; (b) interface isotherms showing HTWs travelling from the lower-left (cold wall) to the upper-right (hot wall) corner. ($t = 5.572 \times 10^5$). The parameters are the same as in FIG. 4.

For a generic variable ϕ, we define the local value of its disturbance ϕ' at the interface (deviation from the base state) as follows,

$$\phi' = \phi - \frac{1}{A_w}\int_{-\frac{A_W}{2}}^{\frac{A_W}{2}} \phi \, \mathrm{d}y \tag{20}$$

where $\phi = T, u, v, w$ or z_i.

The spatial growth of the instabilities is illustrated by several snapshots in FIG. 6. Initially, we observe a group of well-defined HTWs growing near the hot wall and propagating in the negative x and y directions (FIG. 6a). This mode is directly related to the most unstable mode in the linear regime predicted by SD [5] and we shall refer to this group of instabilities as *first HTW mode*. They span around 23% of L when they reach their maximum size and propagate with $\psi = 56°$ with respect to the negative x-axis. Meanwhile the rest of the domain is subject to much weaker disturbances, which are essentially parallel to the x axis. After a certain time, the amplitude of the disturbances grows and the system enters in the non-linear regime. The first HTW mode interacts with other unstable modes and this interaction results into a new front of HTWs that appears near the centre of the liquid

layer travelling from the lower-left to the upper-right corner of the domain (FIG. 6b). At first, the new HTWs grow against the first HTW mode not being strong enough to disrupt it significantly. However, after a while their amplitude grows and the new waves start to overwhelm the first as shown in FIG. 6c. Eventually, the latter perturbation mode dominates the former and the flow reaches an oscillatory state wherein the new HTWs fill the domain completely (FIG. 6d). This new group of HTWs, termed the *prevailing HTW mode*, propagates at $\psi = 55°$ from the negative x-axis.

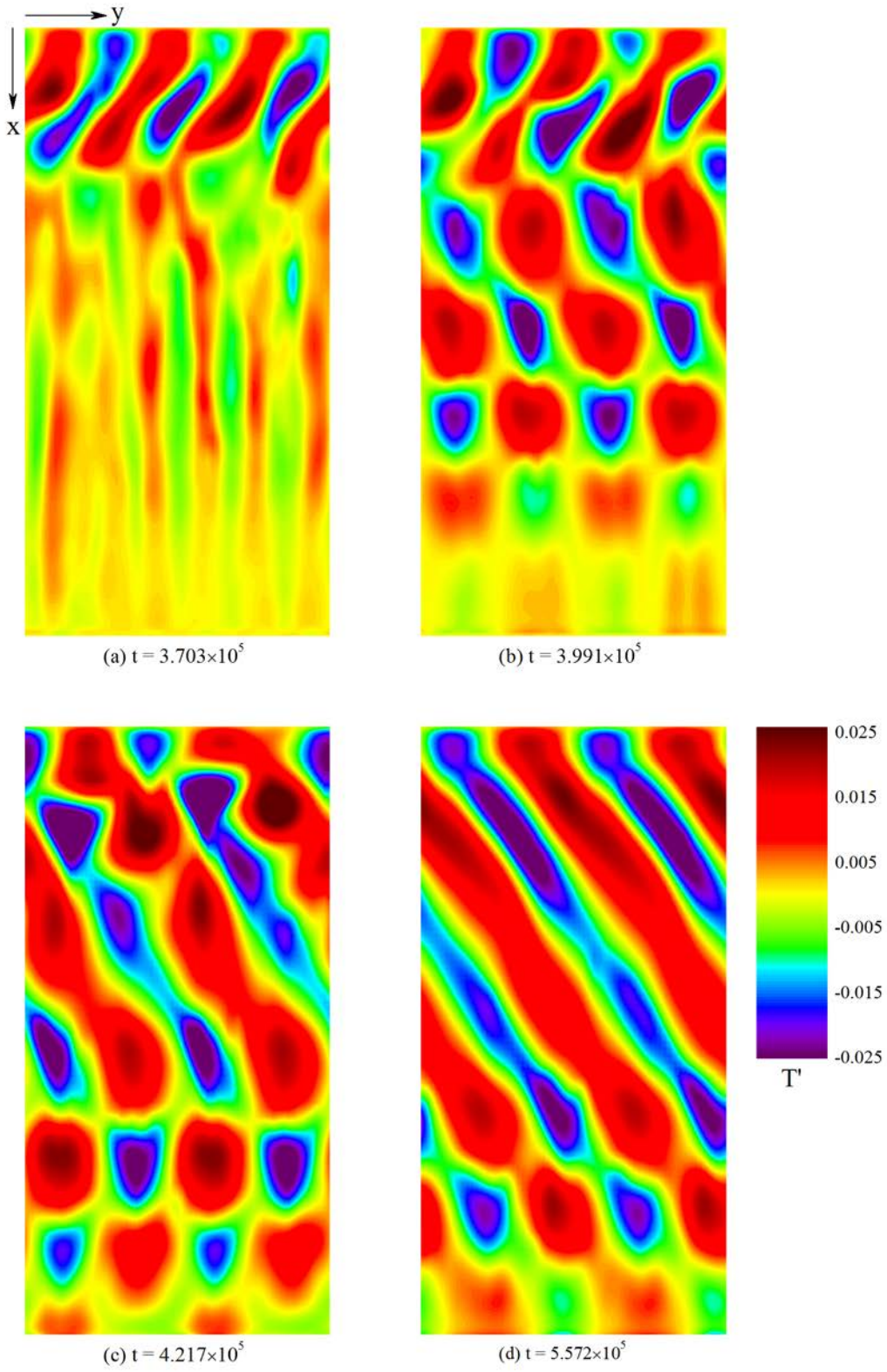

FIG. 6. Contour plots of interface temperature disturbance T' computed at various points in time showing the spatio-temporal growth of the HTWs. (a) First HTW mode near the hot wall ($t = 3.703 \times 10^5$); (b) prevailing HTW mode growing stronger in the centre of the domain ($t = 3.991 \times 10^5$); (c) prevailing HTW mode disrupting the first mode ($t = 4.217 \times 10^5$); (d) prevailing HTW mode fully developed propagating towards the upper-right corner at $\psi = 55°$ with respect to the

negative x axis ($t = 5.572 \times 10^5$). The parameters are the same as in FIG. 4.

HTWs can be characterized by their angle of propagation, ψ, overall wavenumber k and phase-speed c_R. SD [5] obtain these parameters from their linear stability analysis. For the current case, the resulting values are listed in TABLE II along with those found for the *first* and *prevailing* HTW modes shown in FIG. 6; there is generally good agreement for both cases, particularly for ψ.

TABLE II. Comparison between the HTWs predicted by SD [5] and those found in the present investigation for $Pr = 0.75$. First and prevailing modes are those shown in FIG. 6. (*SD's dimensionless framework, ** This is a non-linear wave)

	Smith and Davis [5]	First HTW mode	Prevailing HTW mode
ψ	57°	56°	55°
k	1.52	1.55	1.04**
c_R	0.060	0.090*	0.099*

It is important to study the implications of having periodic boundary conditions in the spanwise direction on the growth of HTWs. Garnier *et al.* [18], for instance, noted this in their investigation with annular geometries. Periodic boundary conditions are employed to minimize the effects of the sidewalls but its use restricts the number of possible HTWs in the *y*-direction to an integer value. For the case under consideration, the wavenumber in the spanwise direction predicted by SD [5] is $\beta = 1.27$, which corresponds to a wavelength of $\lambda_y = 4.95$. The width of the domain is selected so that three of these HTWs can exist $(A_W = 3\lambda_y)$. The good agreement observed for the *first* HTW mode indicates that this group of waves are exactly those reported by SD. However, as the flow evolves into the non-linear regime, the number of waves in the spanwise direction for the *prevailing* mode is only two; the wavenumber becomes $k = 1.04$ as opposed to 1.52 expected from SD. Although *a priori* conceivable, given that SD's theory is not rigorously valid within the non-linear stage, the fact that only a discrete set of possible wavenumbers is possible could indicate that this difference might not be the same for the infinite case wherein there is no constrain derived from spanwise periodicity. To ensure independence from the boundary conditions and

domain's width, we compute the same case with $A_W = 6\lambda_y$ and observe that the number of waves is exactly double for both the *first* and the *prevailing* modes (FIG. 7).

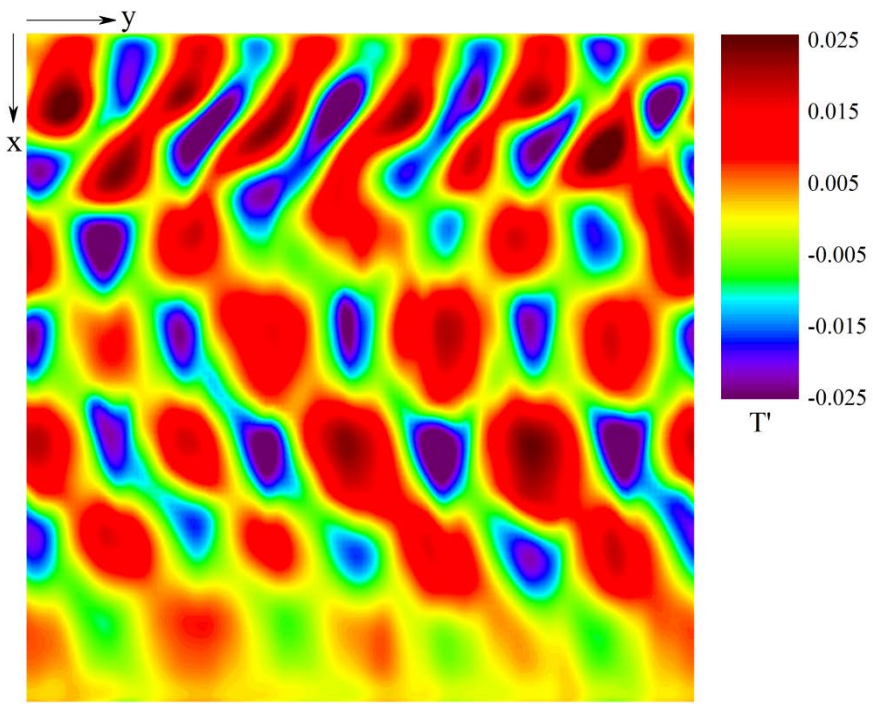

FIG. 7. Frist and prevailing HTW modes observed in a wider domain ($A_W = 30$) with $t = 4.169 \times 10^5$. The rest of the parameters are the same as in FIG. 4.

In addition to the detailed validation against SD as shown above, we present a brief summary of our comparisons against some quasi-numerical studies reported in literature. Parmentier *et al.* [11] carried out a stability analysis, analogous to that of SD, including the effect of buoyancy characterised by a Rayleigh number, Ra. For cases with $Pr = 0.1$ and $Pr = 1$ and with $Ra = 23.4$, which corresponds to the case considered here, the wavenumber is expected to be between $k{\sim}0.7$ for $Pr = 0.1$ and $k{\sim}1.1$ for $Pr = 1$ (Parmentier *et al.* do not present data for $Pr = 0.75$). These values suggest an approximate wavenumber $k{\sim}1$ for our chosen liquid, which compares better with the prevailing mode than the linear SD mode. The authors also report $\psi{\sim}80°$ for $Pr = 0.1$ and $\psi{\sim}52°$ for $Pr = 1$ resulting in an estimated value of $\psi{\sim}60°$ for our liquid; this is in good agreement with the SD results and those presented in our paper. Garr-Peters [10] also discussed the effect of gravity for liquids with $0.01 \leq Pr \leq 10$, this time by means of Bo_d. As in the previous case, k and ψ are assessed with the help of the curves available for the two closest liquids for which $Pr = 0.023$ and 2.22. The wavenumber ranges from $k{\sim}0.35$ for $Pr = 0.023$ to $k{\sim}1$

for $Pr = 2.22$ with an estimated value of $k \sim 0.6$ for the Pr value corresponding to our case, whereas the angle of propagation is expected to be within the range $\psi \sim 64°$ for $Pr = 2.22$ to $\psi \sim 77°$ for $Pr = 0.023$. It is important to note that, in our case, gravity plays only a very minor role in comparison with that of thermocapillarity. Mercier and Normand [12] only considered the case of $Pr = 7$ and controlled the relative importance of buoyancy and thermocapillarity with the ratio $W = Ma/Ra$; here $W = 9$. Comparisons between their analysis and SD's reveal a slight increment in the wavenumber and a noticeable reduction in the angle of propagation when the effect of gravity is weak. SD report $k = 2.58$ and $\psi = 27°$ for $Pr = 7$ and $W = \infty$ (gravity is neglected) while, for the closest case with $W = 8$, Mercier and Normand [12] compute $k = 2.62$ and $\psi = 46°$. Though the transition between stationary and oscillatory modes experimentally observed by Daviaud and Vince [38] was correctly reproduced, the angle of propagation; $\psi \cong 80°$ was not. It must be noted that the cases above ignore the presence of full gas phase dynamics (unlike this work), and mainly deal with much higher Pr than the focus of this work. Hence, a detailed comparison with other semi-numerical work is not possible. We now present an in-depth analysis of the linear and non-linear growth of the thermocapillary and interfacial instabilities.

2. Oscillatory regime - Fourier analysis

The instability's growth is investigated by means of fast Fourier transforms (FFT) performed over the temperature T' and interface height z_i' disturbances. For the time being, we restrict ourselves to the *prevailing* HTWs. FIG. 8 shows the instantaneous evolution of the three most significant sinusoidal modes resulting from the FFT algorithm for the spanwise section across the $x = 0$ plane. It should be noted that this graph has been obtained by carrying out a FFT at every point it time therefore allowing the transient tracking of the fundamental modes.

Initially, the amplitudes of the three leading modes for both T' and z_i' is approximately equal (FIG. 8a-c). This behaviour changes at the HTW's onset, around $t = 3.7 \times 10^5$, and, when the flow is fully-developed, we find the HTWs are essentially coupled thermal perturbations and interface deformations.

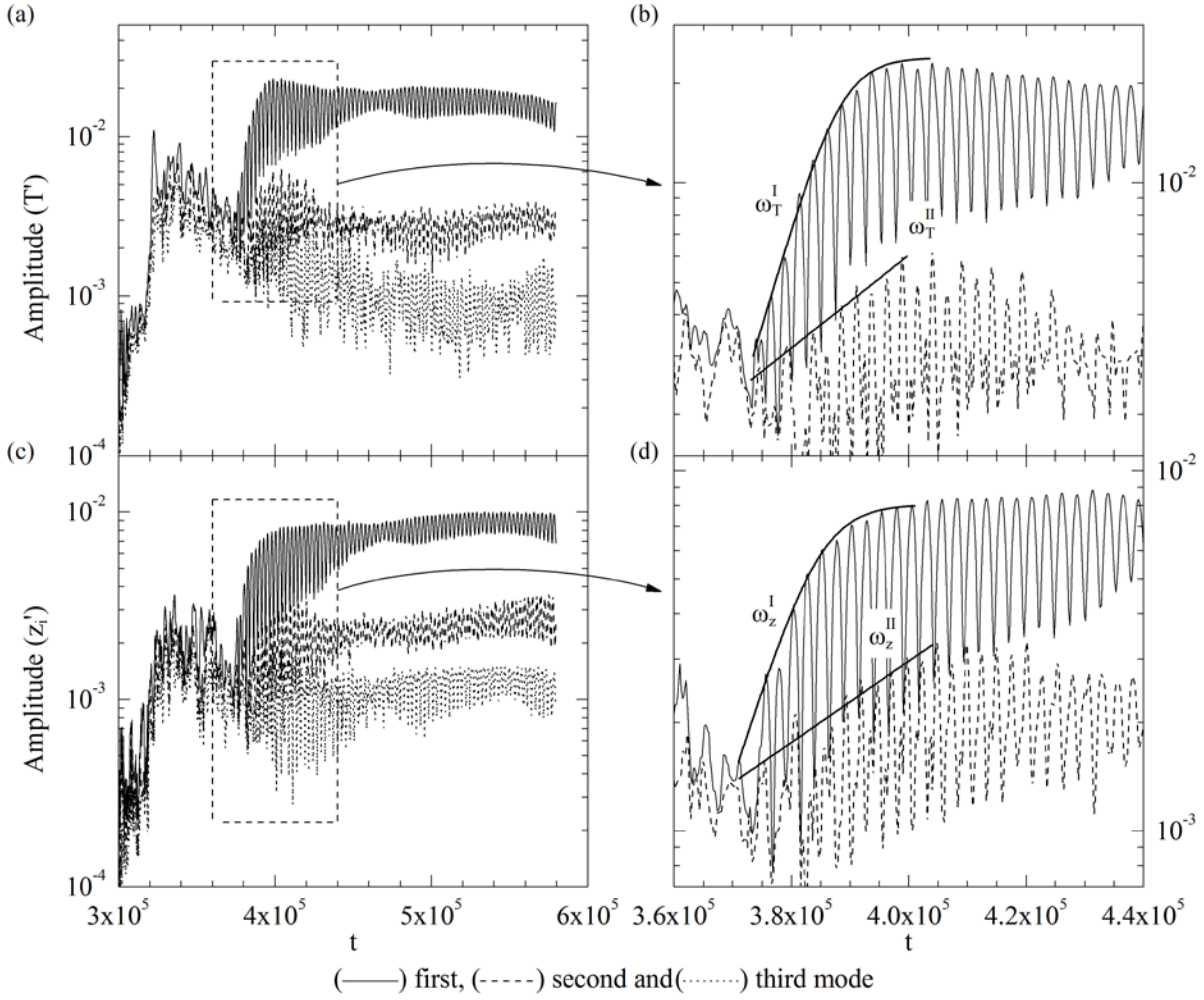

FIG. 8. Instantaneous FFT analysis of the (a) temperature T' and (c) interface height z_i' disturbances for the spanwise section with $x = 0$. Graphs (b) and (d) show a more detailed view of the HTWs' growth phase. The linear growth rates are represented by ω_T^I and ω_T^{II} for T' and by ω_z^I and ω_z^{II} for T'. The parameters are the same as in FIG. 4.

Of most interest is the HTW's growth phase shown in detail in FIG. 8b and d. The third mode (least relevant) has been left out for the sake of clarity. FIG. 8b and d show regions of linear growth for both sinusoidal modes from T' and z_i'. The actual growth rate for each mode is calculated by fitting exponential functions of the type $\varphi(t) = \varphi_0 \cdot e^{\omega t}$ (FIG. 8b-d). We find that the growth rates for first and second modes are $\omega_T^I = 1.4 \times 10^{-4}$ and $\omega_T^{II} = 3.23 \times 10^{-5}$ for T' and $\omega_z^I = 1.2 \times 10^{-4}$ and $\omega_z^{II} = 2.6 \times 10^{-5}$ for z_i'. Calculation of their respective ratios yields $\omega_T^I/\omega_T^{II} = 4.3$ and $\omega_z^I/\omega_z^{II} = 4.6$ which are remarkably close suggesting that the temperature and interfacial waves are strongly connected. Overtones are enslaved to the fundamental mode.

The study of the HTWs' spatial growth is continued by plotting the instantaneous T' and z_i' at P_o and at two additional monitoring points P_c and P_h situated near the cold and hot wall respectively. The horizontal coordinates of these new locations are $(x_{P_c}, y_{P_c}) = (13.5, 0)$ and $(x_{P_h}, y_{P_h}) = (-13.5, 0)$. We find that the HTWs do not grow uniformly in either space or time (FIG. 9). The prevailing HTWs are first observed in P_h, P_o and P_c at $t = 3.4 \times 10^5$ (aprox.), 3.7×10^5 and 4.1×10^5 respectively, which confirms that the HTWs spatially grow in the opposite direction to that they propagate. Towards the hot wall both the disturbance growth rate and its final amplitude are larger. FIG. 9b shows the instantaneous interface height disturbance at the same points revealing that the gas-liquid interface presents its largest deformations at the domain's centre. From these graphs it is also clear the existence of a direct relationship between the growth of the HTWs and the interface deformations.

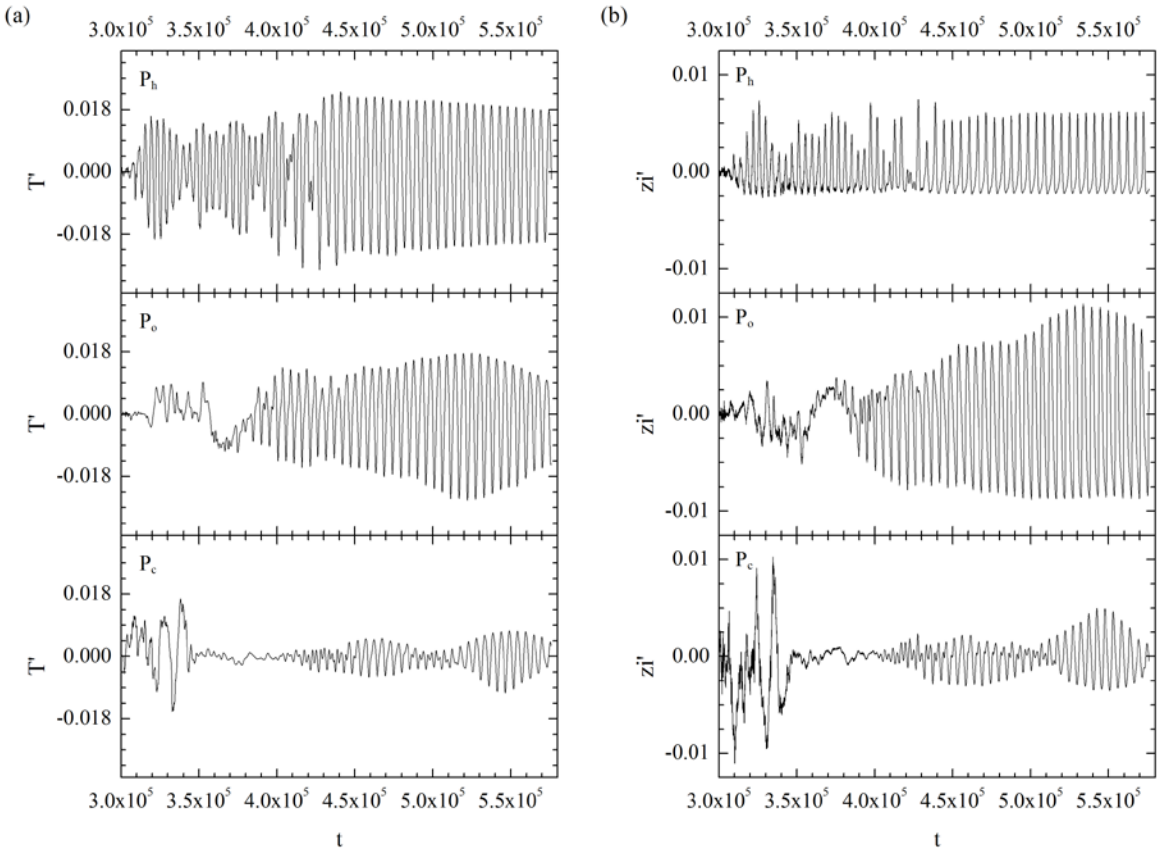

FIG. 9. Instantaneous evolution of the (a) temperature T' and (b) interface height z_i' disturbances at monitoring points near the hot wall (P_h), centre of the layer (P_o) and near the cold wall (P_c). The parameters are the same as in FIG. 4.

The FFT analyses of the T'signals, shown in FIG. 9a, result in the plot shown in FIG. 10a. The temperature disturbance captured by the monitoring locations are essentially a sinusoidal function of frequency $f = 1.88 \times 10^{-4}$. Conversion of this frequency to the SD dimensionless framework results in $f = 7.66 \times 10^{-3}$ which is roughly half of the value reported by SD [5] for the critical mode, $f_c = 14.3 \times 10^{-3}$. In all three cases, the second most important mode is less that 10% of the fundamental. The corresponding amplitudes are 1.85×10^{-2}, 1.42×10^{-2} and 2.87×10^{-3} for P_h, P_o and P_c respectively which is in accordance with the observations made in FIG. 6d or FIG. 9, i.e. increasing HTW strength towards the hot end-wall. A similar plot to FIG. 10a is obtained when we compute the FFT for the z_i' signals, FIG. 10b. In this case, the leading modes act at the same frequency but the strongest is found at the centre of the layer (P_o) with an amplitude of 6.73×10^{-3}. The maximum interface deviation for P_h and P_c is 2.65×10^{-3} and 1.27×10^{-3} respectively.

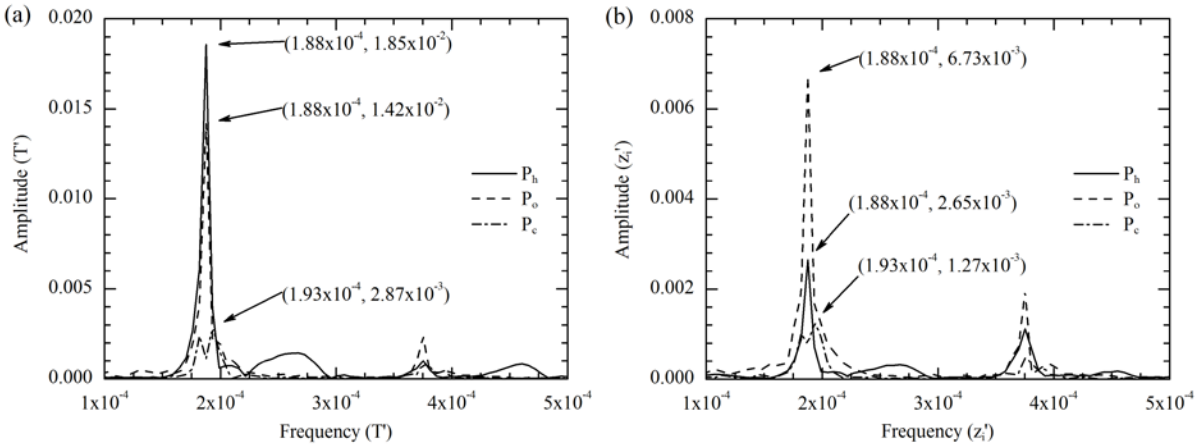

FIG. 10. Frequency/amplitude diagram resulting from the Fast Fourier Transform (FFT) performed over the oscillatory (a) thermal disturbance T' (b) interface-height disturbance z_i' shown in FIG. 9. The parameters are the same as in FIG. 4.

The conclusions drawn from the Fourier analysis are strengthened when we plot together the instantaneous T' and z_i' for one of the points (P_o) and zoom in so we can precisely study a few perturbation cycles, FIG. 11. We observe that T' and z_i' are out-of-phase: a positive thermal perturbation is immediately followed by an interface depression after $t = 0.43\tau$. As it will be explained in more detail when the bulk flow is presented, the relationship between T' and z_i' illustrated in Fig. 10 results from the Marangoni effect for liquids, like the ones considered in the present work, for which the surface tension is inversely dependent on T. A

hot spot in the interface corresponds to a location with lower surface tension than its surroundings which results in the liquid being dragged away from it with the subsequent local level depression becoming deeper. A similar effect is also observed in the case of surfactant-driven thin-film flows in which the surface tension is a decreasing function of the surfactant concentration [39].

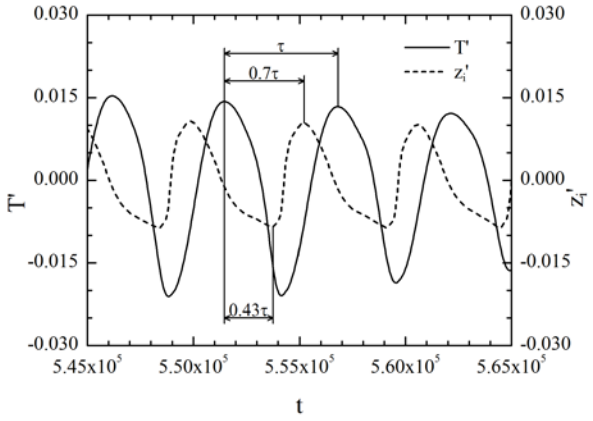

FIG. 11. Instantaneous temperature T' and interface height z_i' disturbances at the centre of the liquid layer within the oscillatory stage, monitoring point P_o. The parameters are the same as in FIG. 4.

FIG. 12 shows the interface disturbance z_i' at the same instant within the oscillatory regime that we investigate in FIG. 5 or FIG. 6d, i.e. $t = 5.572 \times 10^5$. Comparing FIG. 12 with FIG. 6d reveals that that the physical interface deformations follow the HTW pattern, travelling with the same angle of propagation ψ and phase-speed c_R from the lower-left corner (cold wall) towards the upper-right end (hot wall). Thus, we conclude that HTWs are not only travelling temperature perturbations but they also entail interfacial waves.

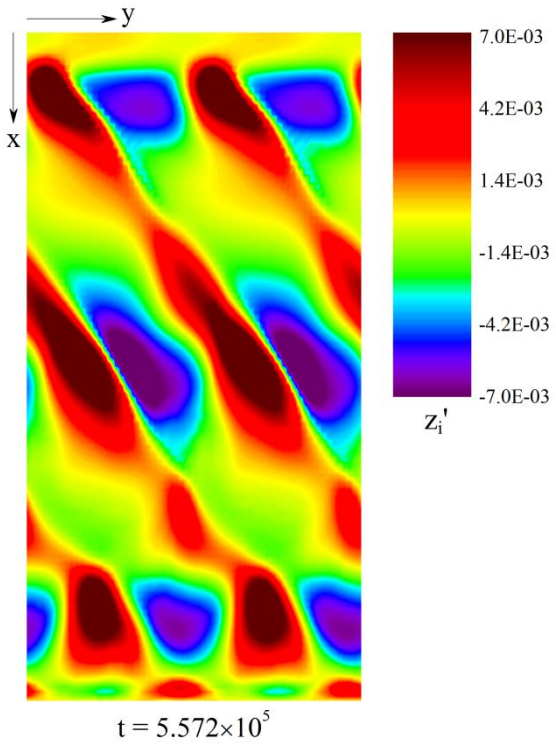

FIG. 12. Interface-height disturbance z_i' at an instant within the oscillatory regime (same as that of FIG. 6d). The parameters are the same as in FIG. 4.

3. Bulk flow

We investigate the bulk flow within the non-linear regime for both liquid and gas phases by considering three vertical sections: one parallel to the *yz*-plane (spanwise section), another parallel to the *xz*-plane (streamwise section) and a third section perpendicular to the HTW front, as shown in FIG. 13, FIG. 15 and FIG. 16, respectively. These sections are slightly closer towards the hot boundary where the amplitude of the HTWs is larger and better defined. FIG. 13 shows (a) the temperature and interface-height disturbance, (b) the tangential velocity field and (c) the streamline plot for the spanwise section at $x = -6$ and $t = 5.572 \times 10^5$. We observe two fully-formed HTWs travelling in the positive *y* direction and an equal number of interface deformations following them, FIG. 13a. The interface deformations are characterised by sharp crests with wide and nearly horizontal troughs whereas the thermal perturbations are more sinusoidal. The wavenumber in the spanwise direction is $\beta = 0.84$ which is fairly close to the critical value reported by SD [5], $\beta_c = 1.27$, even though we are in the non-linear regime. The spatial delay between T' and z_i' follows the same ratios as those reported in FIG. 11. For example, from FIG. 13a one can see that the

delay between subsequent T' and z_i' crests is approximately 0.7 times the wavelength in the spanwise direction which is in agreement with the temporal delay observed in FIG. 11.

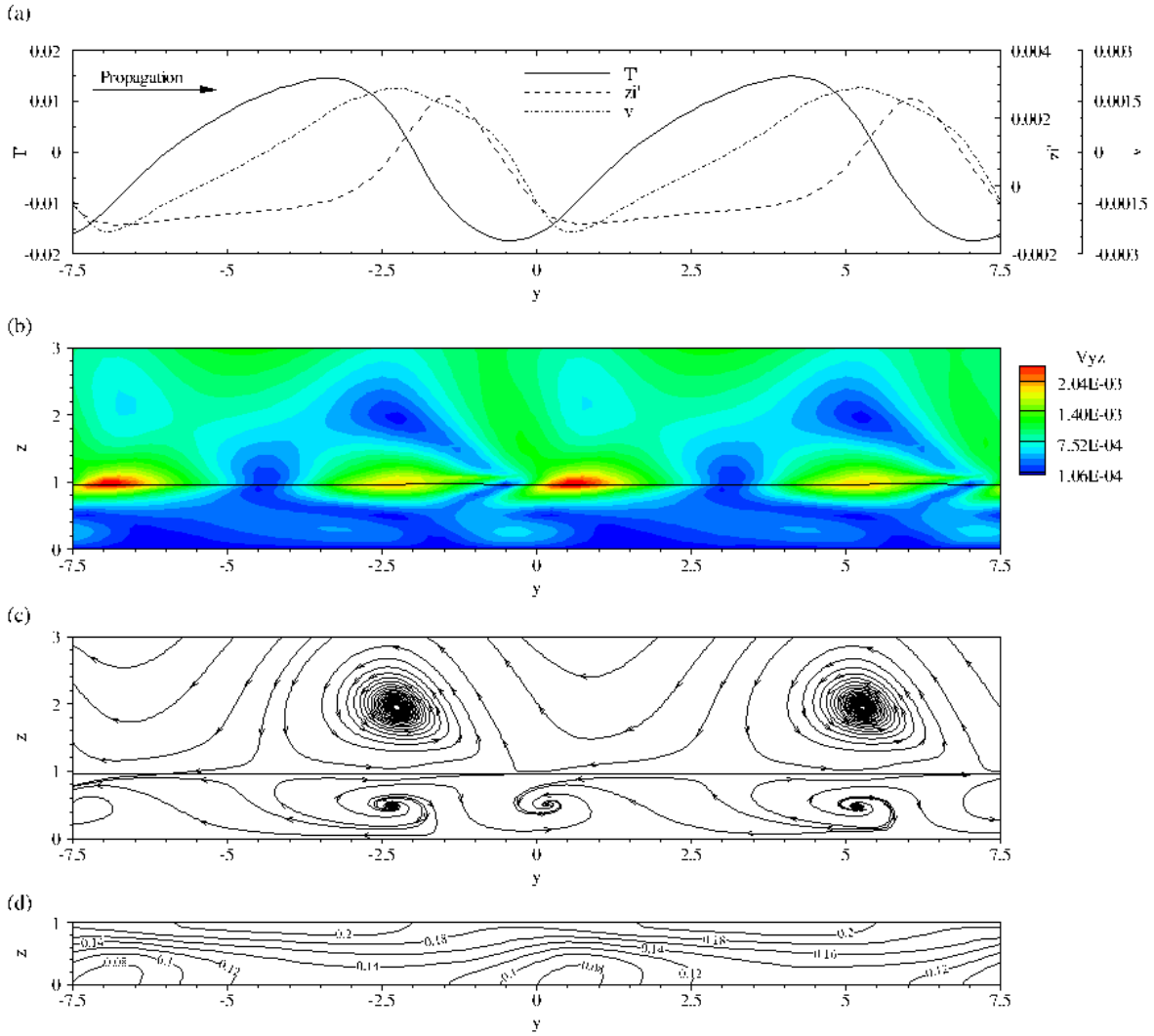

FIG. 13. Spanwise section with $x = -6$ and $t = 5.572 \times 10^5$; (a) thermal and interface-height perturbations and interface velocity; (b) tangential velocity; (c) streamlines; (d) isotherms. The parameters are the same as in FIG. 4.

The spanwise bulk velocity field is presented in FIG. 13b. The average velocity in the gas is larger than in the liquid. At the interface the flow is being pulled due to the Marangoni effects towards cold spots (min T') from both sides which causes these points to be locations where opposite fluid streams collide and consequently where the velocity is minimum. The velocity of the interface fluid travelling towards the cold spots in the negative y direction (opposite to the HTW propagation) is higher than in the contrary case. These velocity inequalities result from energy imbalances around the cold spots. More thermal energy is

transported from the hot spots towards their downstream cold points (negative y direction) than from the hot spots to their preceding cold ones. The net result is that the temperature at cold spots rises as the following hot spots become colder and the HTWs propagate spatially in the positive y. FIG. 13c shows the streamlines for both phases. Very well formed rolls rotating counter-clockwise are observed in the gas phase. These rolls follow the HTWs at the same velocity and their centre is located $0.24\lambda_y$ and $0.11\lambda_y$ after the points of minimum T' and maximum z_i' respectively, and are due to transport of momentum from the liquid phase through the interfacial stress. The streamline sources and sinks observed in the liquid are nothing but the projection of oblique rolls travel with the HTWs. These are explained in detail in FIG. 15 and FIG. 16.

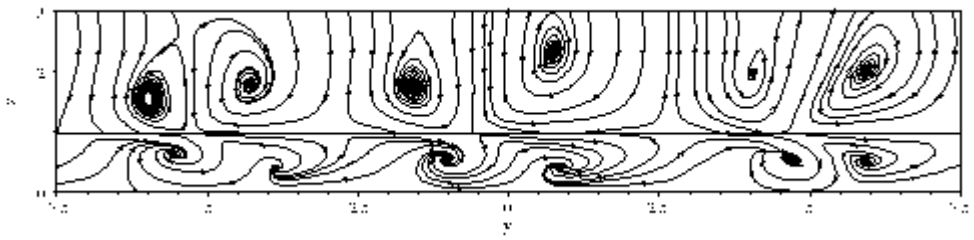

FIG. 14. Streamlines at $t = 3.703 \times 10^5$ for a spanwise plane with $x = -10$. The point in time is the same as in FIG. 6a; the HTWs propagate towards the negative y direction. The parameters are the same as in FIG. 4.

FIG. 14 shows the spanwise streamlines for the *first* HTW mode found at $t = 3.703 \times 10^5$ (FIG. 6a). This mode exists for a relatively long period of time and then is suppressed by the *prevailing* disturbance at later times; however, it bears similarities to the *prevailing* HTW. Here, we observe three pairs of counter-rotating rolls in the gas travelling with the HTWs. As the simulation evolves, the size of the rolls rotating in one direction grows while the gap available for the second set of rolls becomes smaller. The result is that one set of rolls remains next to the interface and the other is pushed upwards. This behaviour and the shape of the velocity field between rolls in FIG. 13 lead us to think that there is a second layer of rolls in the gas phase rotating clockwise and located between those shown in FIG. 13 at a higher level. The flow in the liquid phase is comparatively slower and it also presents a characteristic pattern composed of swirls' pairs travelling with the HTWs (FIG. 13c).

FIG. 15 shows a streamwise section, at y = 0, in which the HTWs travel upstream, and the delays between T' and z_i' signals maintain the ratios reported in FIG. 11 and FIG. 13. The

wavenumber in the streamwise direction is $\alpha = 0.62$, which compares well with critical wavenumber $\alpha_c = 0.82$ obtained from the linear theory by SD [5]. The interface-deformation profile is again formed by relatively wide valleys and narrower crests. The flow is driven by surface tension gradients at the interface, hence convection is stronger there. We observe the same imbalance between the velocities around cold spots that leads to the HTW propagation.

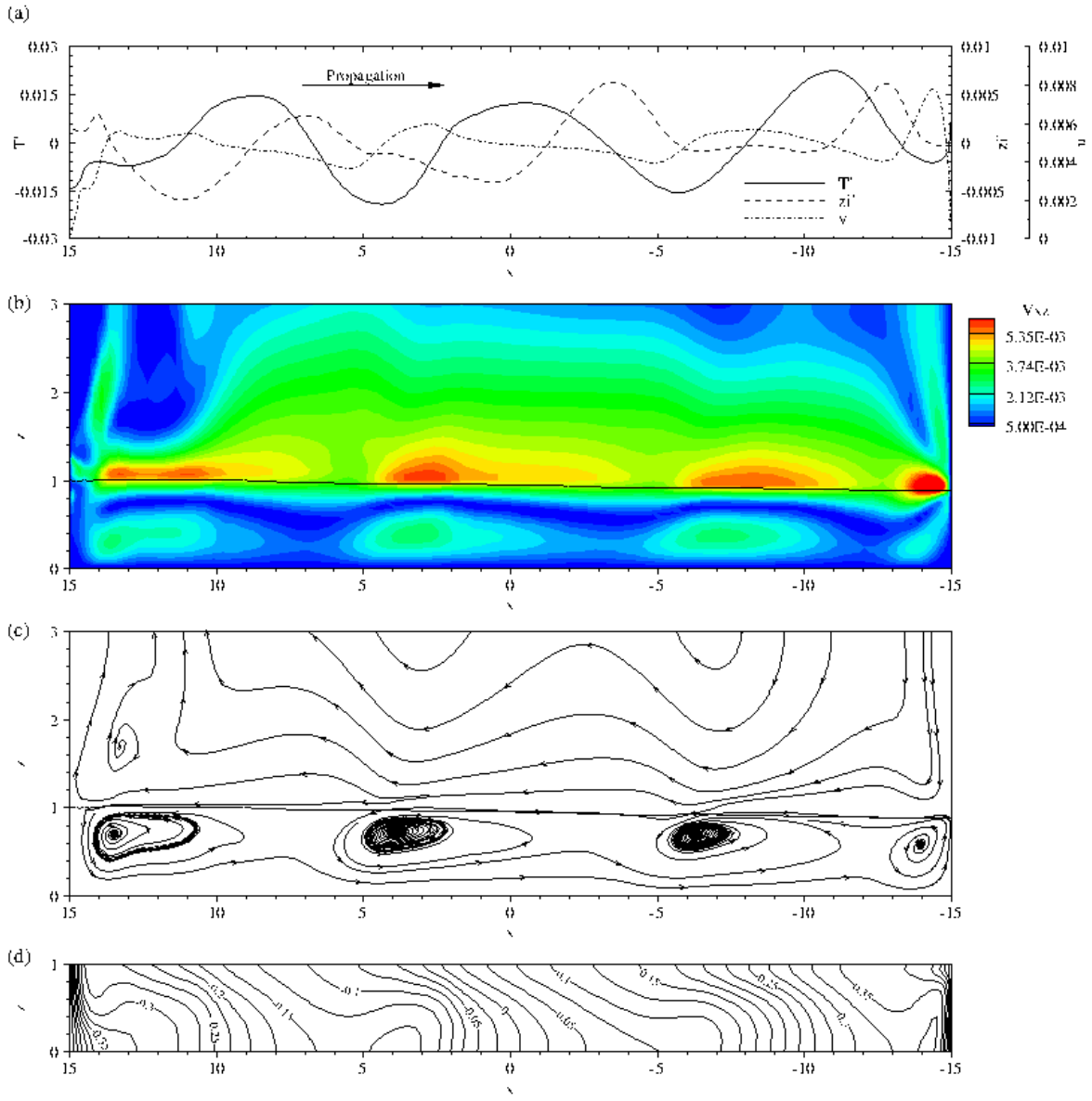

FIG. 15. Streamwise section across the centre of the domain $y = 0$ with $t = 5.572 \times 10^5$; (a) thermal and interface-height perturbations and interface velocity; (b) tangential velocity field; (c) streamlines; (d) isotherms. The vertical dimension is scaled up by a factor of 3 with respect to x in (b), (c) and (d) for clarity of presentation. The parameters are the same as in FIG. 4.

Moving at higher velocity than the liquid $(\Gamma_\mu > 1)$, the gas motion presents a wavy pattern (FIG. 15c) resulting from the projection of the oblique rolls observed in the spanwise

section (FIG. 13b) onto the streamwise plane. The main stream enters the domain through the open boundary near the hot wall and leaves it at the cold boundary. Stagnation areas appear near the exit point, where the main flow collides with the solid wall. Alterations to this behaviour are expected for lower Γ_k because buoyancy then will try to drive the gas near the walls in the opposite directions, i.e. buoyancy acts against interfacial convection to drive upwards the hot gas next to the heated boundary (the contrary case will be found near the cold wall).

The analysis of the liquid phase reveals two standing rolls at (and parallel to) the vertical walls along with a second pair of oblique rolls, whose axes are parallel to the HTW fronts, propagating with the thermal disturbances towards the heated boundary. The former result from the inversion of the flow direction at the solid walls whereas the latter are provoked by the HTWs.

The description of the flow under consideration is completed with the study of the section parallel to the direction of propagation across the point $(x, y) = (-6, 0)$, shown in FIG. 16. The data reveals that the amplitude of the thermal disturbance is not constant, but grows in the direction of propagation form 0.0125 to 0.0235. This tendency is also reported by RN in their experimental investigation [14] and it is most likely to be a result of the finite domain. The interface-height disturbance presents the opposite behaviour with its amplitude falling from 0.01 to roughly 0.002. The streamline plot (FIG. 16c) shows the travelling liquid rolls previously reported. Their centres are located just before the coldest spots at a vertical coordinate equal to 2/3 of the local interface height. Note that this position coincides exactly with the point of zero velocity in the base state (FIG. 3a), which is not surprising given that the streamwise velocity field in the core region (FIG. 15b) is basically the base state (return-flow solution) altered by a weaker periodic perturbation superposed. The rotational speed of the rolls rises in the direction of propagation. This is directly derived from the growth of T' observed along the same path which results in larger surface tension gradients (driving force).

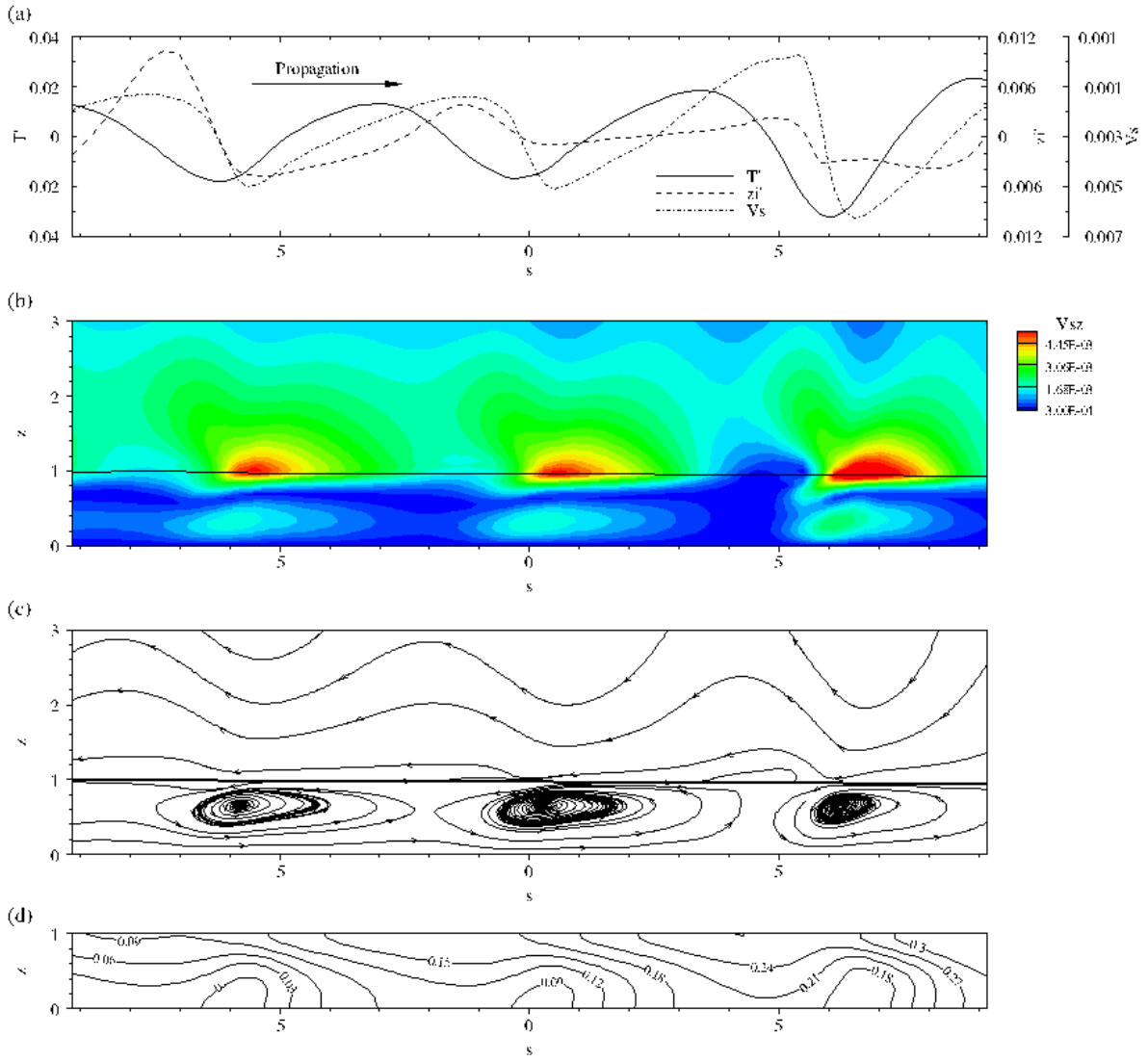

FIG. 16. Vertical section parallel to the direction of propagation across the point $(x, y) = (-6, 0)$ at $t = 5.572 \times 10^5$; (a) thermal and interface-height perturbations and interface velocity; (b) tangential velocity field; (c) streamlines; (d) isotherms. The parameter s denotes the coordinate along the direction of propagation. The vertical dimension is scaled up by a factor of 1.5 with respect to s in (b), (c) and (d) for visualization purposes. The parameters are the same as in FIG. 4.

C. Non-adiabatic interface

To date, thermocapillary instabilities have been numerically investigated by means of single-phase models solely, wherein heat losses across the free surface are computed through the thermal boundary condition acting on it. In most cases, the authors use simple expressions where the heat flux is calculated based on the Biot number $B = hd/k$ and the temperature jump between the local temperature and the temperature of the bounding gas far from the free

surface T_r, i.e. $\partial T/\partial z = -B\,(T - T_r)$. Such expressions are again approximations required when the gas phase is neglected and imply that the heat-flux distribution across the liquid surface is essentially dictated by the streamwise temperature profile rather than by the normal (local) temperature gradient between the liquid at the interface and the gas right next to it. In our model the gas phase dynamics is completely resolved by considering continuity of temperature at the interface, hence we have no need for this type of assumptions. Furthermore, this capability allows us to investigate, for the first time, the role of the local heat transfer across the interface in the HTW mechanism.

We consider the same unstable system to that previously described with the only difference that the gas is not a thermal insulator anymore and, therefore, heat transfer between phases is permitted. To that end, the conductivity ratio is reduced to a reasonable value, $\Gamma_k = 70$, while the remaining dimensionless groups along with the geometrical domain, mesh and marching time are maintained the same. To save computational time, the simulation is started from the results of the case previously presented at an instant after the adjustment period (FIG. 4). For the sake of simplicity, this instant is set as the reference $(t = 0)$.

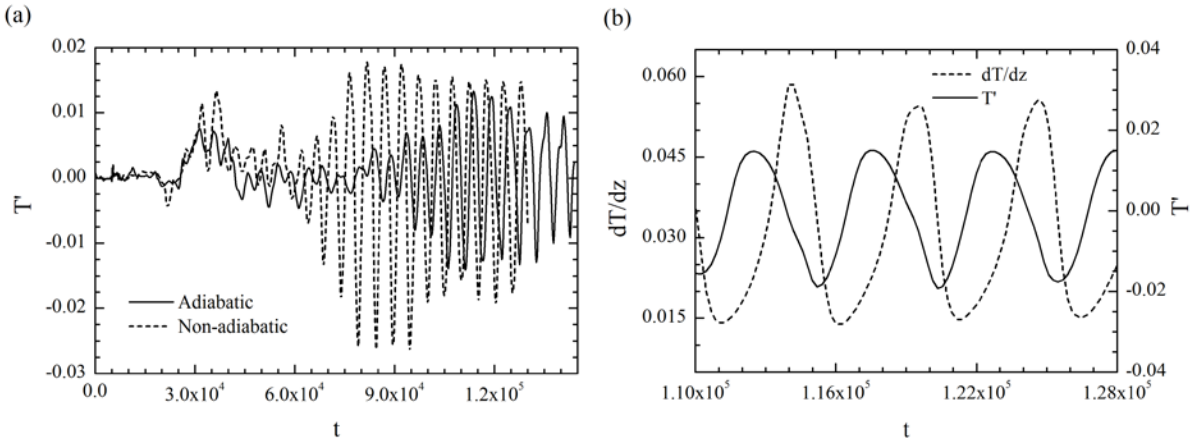

FIG. 17. Instantaneous distribution of (a) T' for the adiabatic and non-adiabatic interface cases; (b) T' and the vertical temperature gradient $\partial T/\partial z$ for the non-adiabatic interface case within the prevailing oscillatory regime; Monitoring point P_o. Parameters: $Pr = 0.75$, $Re = 11912$, $Fr = 1726$, $We = 748$, $Bo_d = 0.111$, $Ma_L = 8934$, $\Gamma_\rho = 641$, $\Gamma_\mu = 14.3$, $\Gamma_k = 70$, $\Gamma_{c_p} = 2$ and $\Gamma_\beta = 0.4$.

FIG. 17a shows the temporal evolution of the temperature disturbance T' at P_o for both the adiabatic and non-adiabatic interface cases. The non-adiabatic system exhibits a similar

transient progress to the adiabatic case (same stages) but the *prevailing* HTW mode develops in a shorter period of time. We compute Ma, direction of propagation, wavenumber and phase-speed, and find that these parameters are essentially the same as those reported for the adiabatic case: $Ma = 210$, $\psi = 55°$, $k = 1.05$ and $c_R = 0.098$. However, FIG. 17a shows the heat transfer across the interface has increased the instability's growth rate and maximum amplitude.

For these observations to be consistent with previous investigations [5], which reported a stabilizing effect of heat loss across the free surface, the gas should warm the liquid. The local net heat flux between phases is given by $q_{net} = -(\mathbf{n} \cdot k\nabla T)$, however, when the interface is horizontal, which is essentially our case, only the vertical component of Fourier's law is relevant, i.e. $q_{net} \approx q_z = -k(\partial T/\partial z)$. We compute the temperature gradient at the interface and find that $\partial T/\partial z \geq 0$ everywhere. Thus, we can confirm that the energy indeed flows from the gas to the liquid. The gradient distribution is highly transient and follows the HTW pattern. The maximum values are observed next to the solid walls where the different extensions of the thermal boundaries layers for the liquid and the gas provoke the largest vertical temperature gradients. Our findings agree with the experimental observations by Schwabe *et al.* [17] in which the authors also report heat input to the free surface in an analogous annular system.

FIG. 17b reveals the highly transient behaviour of the local heat flux across the interface. We observe that the maximum gradient does not coincide with the coldest locations and compute a temporal delay of roughly 0.35τ between the hot spots and the subsequent $\partial T/\partial z$ maxima. Note that these findings are again in contradiction with the results obtained with single-phase models which predict the largest energy fluxes at extreme-temperature locations (either crests or troughs depending on the choice of the T_r) and indicate that the disturbances in the temperature field provoked by the HTWs experience a delay as they propagate into the gas phase. FIG. 18 shows the spanwise temperature profile for interface $T(z_i)$ and the gas just above $T(z_i + 0.3)$ at $t = 1.543 \times 10^5$. The plot confirms that temperature field in the gas is subjected to oscillatory fluctuations provoked by the HTWs. The temperature signals are slightly offset with the gas disturbances following the interface HTWs. This delay explains why the maximum heat fluxes occur between temperature crests. The amplitude of the temperature perturbations becomes weaker as they travel away from the interface until a

point where they are completely dissipated. This spatio-temporal delay leads to the oscillatory behaviour of the heat flux (FIG. 17b).

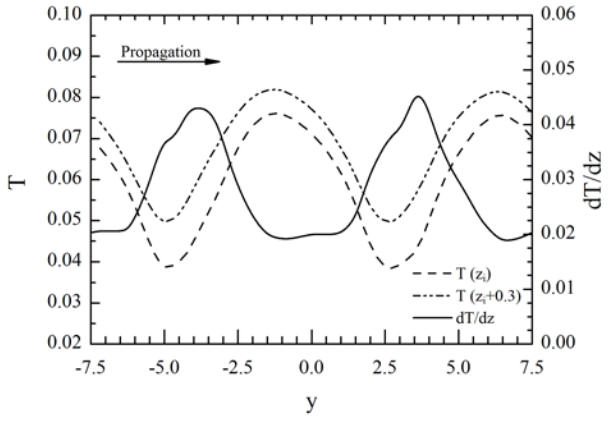

FIG. 18. Spanwise section at $x = 0$ showing the temperature profile for the interface $T(z_i)$, for the gas just above the interface, $T(z_i + 0.3)$, and the resulting vertical gradient dT/dz. The parameters are the same as in FIG. 17.

IV. CONCLUSIONS

The hydrothermal-wave instability first predicted by SD [5] has been investigated by means of two-phase direct numerical simulations of shallow liquid layers surrounded by saturated environments. Imposition of a horizontal temperature gradient along the interface between the liquid and the gas results in thermocapillary motion. We have studied this problem employing novel direct numerical simulations of two-phase flow and heat transfer based on the VOF method in 3D. Our findings show the benefits of this novel strategy capable of capturing interface deformations as well as solving the coupled behaviour of the gas phase.

The numerical results have been validated against the original linear-stability theory by SD [5] and the experimental work by RN [14] concluding excellent agreement in both cases. Obliquely travelling HTWs have been reported for a liquid with $Pr = 0.75$ and a gas acting as a thermal insulator. The HTWs' angle of propagation, wavenumber and phase-speed have been computed and compared to the values predicted by SD [5] obtaining good agreement. We have extensively described the instability's onset and growth revealing complex spatio-

temporal evolution. It has been observed that unstable systems give rise to not only thermal disturbances on the base state (HTWs) but also induce interface deformation (physical waves). These physical waves follow the HTW pattern travelling with the same angle of propagation but with a phase-lag. We have paid special attention to the non-linear growth of instabilities' by means of a Fourier analyses to investigate the relationships between the hydrothermal and physical waves (FIG. 8). The linear-growth regions have been identified for the first two fundamental sinusoidal modes in both disturbances and the actual growth rates have been computed by fitting exponential functions. We find that the ratios between the growths rate of the fundamental modes to the first overtones follow the same ratio for both the thermal and the physical waves, suggesting a strong link between the two and also that the overtones are enslaved to the fundamental mode. To the best of our knowledge, this is the first time that interface deformations coupled with the HTWs have been reported.

In the third part of our work, we have described the main features of the bulk flow for both liquid and gas phases using the principal vertical sections, that is to say a spanwise (FIG. 13), a streamwise (FIG. 15) and a section perpendicular to the HTWs' front (FIG. 16). Convective rolls have been reported in both phases along with their coupled behaviour with the interface temperature and interface-height disturbances.

Finally, we have taken advantage of our model, which solves the interfacial energy balance using the local conditions of both fluids, to investigate the mechanism of heat transfer between phases. We have proved that single-phase or the so-called one-sided approaches to model this phenomenon via the temperature gradient between the interface and a constant reference temperature (room temperature) provide imprecise results. The travelling nature of the HTWs leads to a delay in the propagation of thermal perturbations towards the gas phase which results in maximum heat fluxes not at the points of highest temperatures but somewhere in between.

V. ACKNOWLEDGMENTS

PJS is grateful to the Fundación Caja Madrid & EPSRC Doctoral Training Grant (EP/P50550X/1) who funded this work.

VI. REFERENCES

1. H. Bénard, *The cellular whirlpools in a liquid sheet transporting heat by convection in a permanent regime.* Annales De Chimie Et De Physique, 1901. **23**: p. 62-101.

2. L. Rayleigh, *On convection currents in a horizontal layer of fluid, when the higher temperature is on the under side.* Philosophical Magazine, 1916. **32**(187-92): p. 529-546.

3. J.R.A. Pearson, *On Convection Cells Induced by Surface Tension.* Journal of Fluid Mechanics, 1958. **4**(5): p. 489-500.

4. L.E. Scriven and C.V. Sternling, *On Cellular Convection Driven by Surface-Tension Gradients - Effects of Mean Surface Tension and Surface Viscosity.* Journal of Fluid Mechanics, 1964. **19**(3): p. 321-340.

5. M.K. Smith and S.H. Davis, *Instabilities of Dynamic Thermocapillary Liquid Layers .1. Convective Instabilities.* Journal of Fluid Mechanics, 1983. **132**(Jul): p. 119-144.

6. M.K. Smith and S.H. Davis, *Instabilities of Dynamic Thermocapillary Liquid Layers .2. Surface-Wave Instabilities.* Journal of Fluid Mechanics, 1983. **132**(Jul): p. 145-162.

7. S.H. Davis, *Thermocapillary Instabilities.* Annual Review of Fluid Mechanics, 1987. **19**: p. 403-435.

8. M.K. Smith, *Instability Mechanisms in Dynamic Thermocapillary Liquid Layers.* Physics of Fluids, 1986. **29**(10): p. 3182-3186.

9. J.M. Garr-Peters, *The Neutral Stability of Surface-Tension Driven Cavity Flows Subject to Buoyant Forces .1. Transverse and Longitudinal Disturbances.* Chemical Engineering Science, 1992. **47**(5): p. 1247-1264.

10. J.M. Garr-Peters, *The Neutral Stability of Surface-Tension Driven Cavity Flows Subject to Buoyant Forces .2. Oblique Disturbances.* Chemical Engineering Science, 1992. **47**(5): p. 1265-1276.

11. P.M. Parmentier, V.C. Regnier, and G. Lebon, *Buoyant-Thermocapillary Instabilities in Medium-Prandtl-Number Fluid Layers Subject to a Horizontal Temperature-Gradient.* International Journal of Heat and Mass Transfer, 1993. **36**(9): p. 2417-2427.

12. J.F. Mercier and C. Normand, *Buoyant-thermocapillary instabilities of differentially heated liquid layers.* Physics of Fluids, 1996. **8**(6): p. 1433-1445.

13. C.F. Chan and C.L. Chen, *Effect of gravity on the stability of thermocapillary convection in a horizontal fluid layer.* Journal of Fluid Mechanics, 2010. **647**: p. 91-103.

14. R.J. Riley and G.P. Neitzel, *Instability of thermocapillary-buoyancy convection in shallow layers. Part 1. Characterization of steady and oscillatory instabilities.* Journal of Fluid Mechanics, 1998. **359**: p. 143-164.

15. J. Burguete, N. Mukolobwiez, F. Daviaud, N. Garnier, and A. Chiffaudel, *Buoyant-thermocapillary instabilities in extended liquid layers subjected to a horizontal temperature gradient.* Physics of Fluids, 2001. **13**(10): p. 2773-2787.

16. D. Schwabe, U. Moller, J. Schneider, and A. Scharmann, *Instabilities of Shallow Dynamic Thermocapillary Liquid Layers.* Physics of Fluids a-Fluid Dynamics, 1992. **4**(11): p. 2368-2381.

17. D. Schwabe, A. Zebib, and B.C. Sim, *Oscillatory thermocapillary convection in open cylindrical annuli. Part 1. Experiments under microgravity.* Journal of Fluid Mechanics, 2003. **491**: p. 239-258.

18. N. Garnier, A. Chiffaudel, and F. Daviaud, *Hydrothermal waves in a disk of fluid.* Dynamics of Spatio-Temporal Cellular Structures: Henri Benard Centenary Review, 2006. **207**: p. 147-161.

19. M.F. Schatz and G.P. Neitzel, *Experiments on thermocapillary instabilities.* Annual Review of Fluid Mechanics, 2001. **33**: p. 93-127.

20. J.Y. Xu and A. Zebib, *Oscillatory two- and three-dimensional thermocapillary convection.* Journal of Fluid Mechanics, 1998. **364**: p. 187-209.

21. E. Bucchignani, *Numerical characterization of hydrothermal waves in a laterally heated shallow layer.* Physics of Fluids, 2004. **16**(11): p. 3839-3849.

22. Y.R. Li, L. Peng, Y. Akiyama, and N. Imaishi, *Three-dimensional numerical simulation of thermocapillary flow of moderate Prandtl number fluid in an annular pool.* Journal of Crystal Growth, 2003. **259**(4): p. 374-387.

23. B.C. Sim, A. Zebib, and D. Schwabe, *Oscillatory thermocapillary convection in open cylindrical annuli. Part 2. Simulations.* Journal of Fluid Mechanics, 2003. **491**: p. 259-274.

24. Y.R. Li, N. Imaishi, T. Azami, and T. Hibiya, *Three-dimensional oscillatory flow in a thin annular pool of silicon melt.* Journal of Crystal Growth, 2004. **260**(1-2): p. 28-42.

25. W.Y. Shi and N. Imaishi, *Hydrothermal waves in differentially heated shallow annular pools of silicone oil.* Journal of Crystal Growth, 2006. **290**(1): p. 280-291.

26. L. Peng, Y.R. Li, W.Y. Shi, and N. Imaishi, *Three-dimensional thermocapillary-buoyancy flow of silicone oil in a differentially heated annular pool.* International Journal of Heat and Mass Transfer, 2007. **50**(5-6): p. 872-880.

27. W.Y. Shi, G.Y. Li, X. Liu, Y.R. Li, L. Peng, and N. Imaishi, *Thermocapillary Convection and Buoyant-Thermocapillary Convection in the Annular Pools of Silicon Melt and Silicone Oil.* Journal of Superconductivity and Novel Magnetism, 2010. **23**(6): p. 1169-1172.

28. G. Karapetsas, O.K. Matar, P. Valluri, and K. Sefiane, *Convective Rolls and Hydrothermal Waves in Evaporating Sessile Drops.* Langmuir, 2012. **28**(31): p. 11433-11439.

29. K. Sefiane, J.R. Moffat, O.K. Matar, and R.V. Craster, *Self-excited hydrothermal waves in evaporating sessile drops.* Applied Physics Letters, 2008. **93**(7).

30. A.M. Mancho and H. Herrero, *Instabilities in a laterally heated liquid layer.* Physics of Fluids, 2000. **12**(5): p. 1044-1051.

31. C.W. Hirt and B.D. Nichols, *Volume of Fluid (Vof) Method for the Dynamics of Free Boundaries.* Journal of Computational Physics, 1981. **39**(1): p. 201-225.

32. R. Scardovelli and S. Zaleski, *Direct numerical simulation of free-surface and interfacial flow.* Annual Review of Fluid Mechanics, 1999. **31**: p. 567-603.

33. C. Ma and D. Bothe, *Direct numerical simulation of thermocapillary flow based on the Volume of Fluid method.* International Journal of Multiphase Flow, 2011. **37**(9): p. 1045-1058.

34. A. Alexeev and A. Oron, *Suppression of the Rayleigh-Taylor instability of thin liquid films by the Marangoni effect.* Physics of Fluids, 2007. **19**(8).

35. A. Alexeev, T. Gambaryan-Roisman, and P. Stephan, *Marangoni convection and heat transfer in thin liquid films on heated walls with topography: Experiments and numerical study.* Physics of Fluids, 2005. **17**(6).

36. J.U. Brackbill, D.B. Kothe, and C. Zemach, *A Continuum Method for Modeling Surface-Tension.* Journal of Computational Physics, 1992. **100**(2): p. 335-354.

37. O. Ubbink and R.I. Issa, *A method for capturing sharp fluid interfaces on arbitrary meshes.* Journal of Computational Physics, 1999. **153**(1): p. 26-50.

38. F. Daviaud and J.M. Vince, *Traveling Waves in a Fluid Layer Subjected to a Horizontal Temperature-Gradient.* Physical Review E, 1993. **48**(6): p. 4432-4436.

39. S. Kumar and O.K. Matar, *On the Faraday instability in a surfactant-covered liquid.* Physics of Fluids, 2004. **16**(1): p. 39-46.